

On the incorporation of a micromechanical material model into the inherent strain method—Application to the modeling of selective laser melting

Isabelle Noll¹ | Thorsten Bartel¹ | Andreas Menzel^{1,2}

¹Institute of Mechanics, TU Dortmund University, Dortmund, Germany

²Division of Solid Mechanics, Lund University, Lund, Sweden

Correspondence

Isabelle Noll, Institute of Mechanics, TU Dortmund University,
Leonhard-Euler-Str. 5, 44227 Dortmund, Germany.
Email: isabelle.noll@tu-dortmund.de

Abstract

When developing reliable and useful models for selective laser melting processes of large parts, various simplifications are necessary to achieve computationally efficient simulations. Due to the complex processes taking place during the manufacturing of such parts, especially the material and heat source models influence the simulation results. If accurate predictions of residual stresses and deformation are desired, both complete temperature history and mechanical behavior have to be included in a thermomechanical model. In this article, we combine a multiscale approach using the inherent strain method with a newly developed phase transformation model. With the help of this model, which is based on energy densities and energy minimization, the three states of the material, namely, powder, molten, and resolidified material, are explicitly incorporated into the thermomechanically fully coupled finite-element-based process model of the micromechanically motivated laser heat source model and the simplified layer hatch model.

KEYWORDS

additive manufacturing, finite element method, inherent strain, multiscale framework, phase transformation

1 | INTRODUCTION

Additive manufacturing (AM) of metallic parts—such as the selective laser melting (SLM) process—has gained high interest in the industry, as it allows the manufacturing of components layer by layer which offers a new design freedom and a production of custom-made assemblies. A detailed representation of the SLM process is illustrated in Figure 1, where a moving laser beam heat source melts powder particles of the corresponding layer according to the defined model. Afterwards, the building platform is lowered and a new layer of powder is applied. This process is conducted until the part is finished. Due to the high temperature impact, the particles melt at first and then solidify after a cooling period, so that a dense part is formed. The layer height and the hatching distance have to be chosen according to the melting pool, so that a complete fusion of neighboring layers and melt lines can be assured. Due to this procedure, complex and in particular coupled thermal, mechanical, and metallurgical processes arise during the production. Especially high temperature gradients caused by the laser beam heat input and phase changes influence the characteristics of the part,

This is an open access article under the terms of the Creative Commons Attribution License, which permits use, distribution and reproduction in any medium, provided the original work is properly cited.

© 2021 The Authors. *GAMM - Mitteilungen* published by Wiley-VCH GmbH.

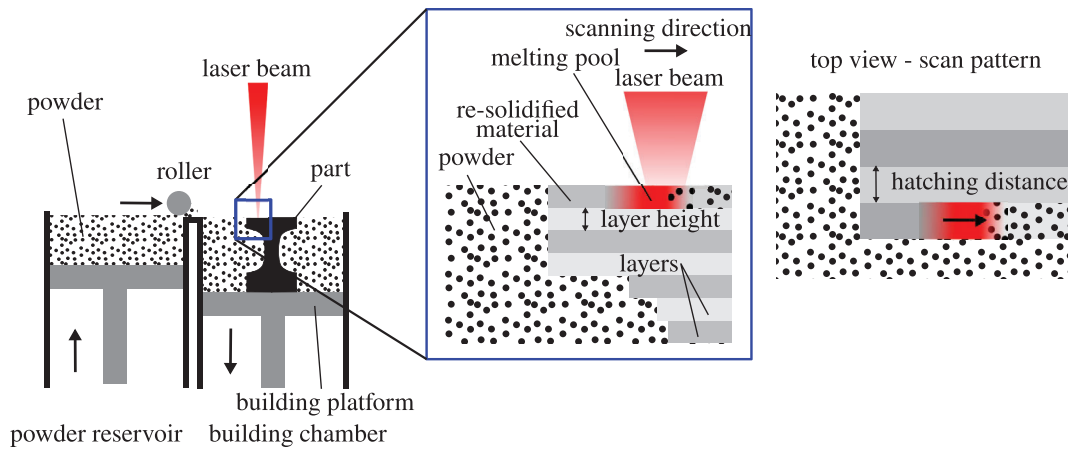


FIGURE 1 Schematic view of the complete selective laser melting process

that is, the mechanical eigenstresses and plastic deformations of the component. Furthermore, the component's quality is highly influenced by the numerous present process parameters.

So far, it is still challenging to predict the characteristics of the manufactured workpieces, for example, the residual stresses and the final deformation, which reduces the ability to use additively manufactured parts in industrial applications. This shows the necessity of simulation tools and appropriate material models, not only on the smaller scales, but also on the macroscale, to gain a deeper understanding of the relation between optimal process parameters and the final part so that time and cost consuming practical trials can be avoided. With proper simulation tools, it is then possible to determine the predeformed shape and optimal building orientation of the part to overcome problems due to warpage and high residual stresses. However, finding appropriate simulation models is a rather challenging task. Besides using suitable material and process models, the computation of finite element (FE) simulations often takes too much computing time. If deformations and eigenstresses are to be predicted, a thermomechanical analysis will be necessary. In addition, a fine mesh needs to be used to properly capture the high temperature gradients of the heat impact which also prolongs the computing time. Therefore, these models without simplifications can only be used for small scale models, where, for example, a single melt line is simulated. However, it is essential to know the geometry changes and residual stresses of real sized parts. Therefore, appropriate choices to reduce the simulation time have to be made. In the present contribution, the focus is set on using a multiscale framework for the SLM process, where three distinct models for the single melt line, the scan island, and the complete part, are considered. This method allows the consideration of different simplifying assumptions regarding the complexity of material models and heat source models, in order to significantly reduce the required computation time for macroscopic simulations. Nevertheless, this method and the part model incorporate physically well motivated assumptions of different material models.

SLM has similar process characteristics as welding when considering the thermal and metallurgical properties. Therefore, the established modeling procedures regarding, for example, heat source models and multiscale frameworks can also be adapted. The inherent strain method (ISM) has been introduced in [37]. Within the weld seam, various thermal expansions and contractions are occurring which lead to residual strains and plastic deformations of the original part. It is assumed that the residual or so-called inherent strains ϵ^{inh} are the reason for these eigenstresses within the final part. This approach has been further developed and applied for welding processes in, for example, [15, 26, 41]. In the latter, the inherent strains are additively decomposed into $\epsilon^{\text{inh}} = \epsilon^{\text{pl}} + \epsilon^{\text{th}} + \epsilon^{\text{cr}} + \epsilon^{\text{trans}}$, representing a plastic, thermal, creep, and transformation contribution, respectively. These strains are extracted from a thermomechanical analysis for one joint and can then be applied to the modeling of the overall welding distortions by using a purely mechanical analysis, where the total strains are determined by an elastic and an inherent contribution, that is, $\epsilon = \epsilon^{\text{el}} + \epsilon^{\text{inh}}$.

Currently, one can differentiate between SLM models based on the ISM and on thermomechanical reduction models. In contrast to welding, multiple passes of the heat source are made during SLM resulting in extensions of these models. A multiscale approach using explicitly a micro-, meso-, and macroscale model is developed in [16,17], where the ISM has been applied for AM—also known as the mechanical layer equivalent. This approach has been applied and compared to experiments in [1], where the residual stresses have been experimentally measured with the contour method. Contrary thereto, the ISM is used in [34, 35], where the inherent strains are determined by measuring test samples. These strains

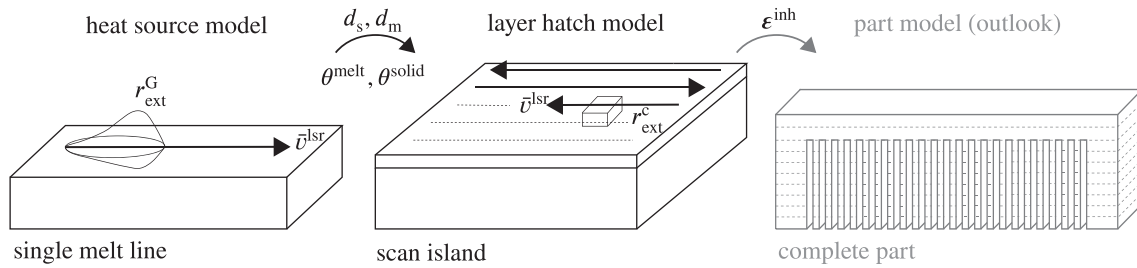


FIGURE 2 Visualization of the three different levels considered in the multiscale approach, where the melt pool dimensions d_s , d_m , temperatures θ^{melt} , θ^{solid} , and the inherent strain ϵ^{inh} are passed from one level to the other

are then applied in mechanical simulations to model the distortion of arbitrary parts. A similar approach is also used in commercial AM software, such as AdditiveLab. However, with this method it is still necessary to construct test samples and measure the deformation of the built specimens for all possible combinations of process parameters. The ISM framework can also be used to determine the necessary pre-deformation of the manufactured part according to the calculated deformation of the original design, compare [17] or to optimize the support structure of a part, f.i., in [44]. An extended ISM is developed in [31], where a phase transformation contribution is added to better predict the behavior of partially austenitic and martensitic steels with evolving phase fractions. In [22], a modified ISM usable for AM has been developed, taking into account two different time states t_1 (intermediate state) and t_2 (steady state) to calculate the final inherent strain $\epsilon^{\text{inh}} = \epsilon_{t_1}^{\text{pl}} + \epsilon_{t_1}^{\text{el}} - \epsilon_{t_2}^{\text{el}}$, which has also been employed in [5].

In literature, various additional simplifications regarding the heat source model, scanning pattern, and layer thickness can be found, where a comprehensive overview is given in [19]. The multiscale approach introduced in [16,17] is advantageous to those methods, where the calculation time is reduced by exposing whole layers at once and by directly combining multiple layers, see, for example, [18, 21, 27, 29, 33, 42], as the scanning strategy cannot be taken into account. Within the literature, models can be found where for example 20 layers [42], or only three layers [29] are merged. A so-called agglomeration approach has been used in [12], where an enlarged layer and beam size is used with an elaborated material model for the solid phase. In this case, the scan strategy of the laser beam is still evaluable to some extent, as the layer is not heated up at once. In [21], a thermomechanical multiscale model regarding the heat source approach is employed to achieve an efficient prediction of the part distortion and the residual stresses. Another method to model large scale parts has been developed in [32], where a sequentially coupled three-dimensional thermal model and two-dimensional mechanical plane stress model is used.

This article is structured as follows: A detailed overview of the multiscale framework based on [16, 17] is given in Section 2, where a focus is set on the employed material and heat source model of the single melt line and scan island. A phase transformation approach as developed in [28] is incorporated for the material model of the heat source model of the single melt line, where each material state—powder, melting pool, and resolidified material—is represented by a specific energy density. In contrast, the melting and solidification temperature directly impacts the present phase of the layer hatch model of the scan island. In Section 3, the implementation of the aforementioned models into the commercial software package Abaqus and the corresponding results are presented. Here, the influence of varying process parameters is examined and discussed, before summarizing our results in Section 4.

2 | MULTISCALE FRAMEWORK

This section provides detailed information regarding the employed multiscale framework. Based on the work of [16, 17], a simulation technique using the FE method shall be developed, where a micromechanically motivated material model is used for the single melt line, but where the overall computational efficiency is increased so that a complete part can be simulated. The multiscale approach as visualized in Figure 2 combines three separate simulations, namely with respect to the micromechanically motivated laser heat source model, the layer hatch model, and the part model; see also Remark 1 in view of the determination of the respective levels of analysis.

The aim of the simulations on the laser heat source model is to calibrate an effective model of the heat source based on a physically sound material model. The results from the heat source model influence the layer hatch model, where the so-called inherent strains are extracted. These are then used to finally specify the part model, which uses

TABLE 1 Comparison of the main characteristics of the three different models considered in the present multiscale approach

Characteristic	Heat source model	Layer hatch model	Part model
Focus	Single melt line	Scan island	Complete part
Size	μm	mm	cm
FEM	Thermomechanical	Thermomechanical	Mechanical
Load	Volumetric Goldak heat source	Cuboid heat source	Mechanical loading
Material model	Phase transformation	Temperature dependent	Elasto-plastic
Material state	Powder, melt, solid	Powder, melt, solid	Solid
Aim	Calibrate heat source	Extract inherent strains	Calculate eigenstresses/deformation

Note: The part model is included for the sake of completeness.

a simpler purely mechanical simulation to compute the residual stresses and deformations of a complete part. With the help of the framework described in the following, it is possible to simulate the AM process of complex macroscopic parts, while the computation time is acceptable. In this work, we present the first steps toward this vision by addressing the single track and single layer simulations. Future work will address the scaling up to the part simulations.

For the laser heat source model, a micromechanically motivated and thermomechanically coupled material model is used for a single melt line, where a volumetric Goldak heat source is applied as external heat supply r_{ext}^G . The aim of the model is to calibrate the geometric parameters of the Goldak heat source corresponding to the laser beam heat input, so that the melt pool geometry of the simulation coincides with the one of experiments. Within the heat source resembling the laser beam, the process parameters laser velocity \bar{v}^{lsr} and laser power P are included. This approach is visualized in Figure 2, left side. Finally, the melt pool dimensions d_s and d_m , describing the width and the depth of the melt pool, respectively, can be extracted from the simulation results.

These outcomes influence the thermomechanically coupled layer hatch model, where a single scan island is simulated, so that the necessary hatching distance w_h and layer thickness h_{lyr} can be evaluated according to the melt pool geometry of the single melt line. A simplified constitutive model is used, where the critical phase transformation temperatures θ^{melt} and θ^{solid} are extracted from the simulation results of the single melt line. The purpose of the model is to extract an averaged inherent strain ϵ^{inh} which can then be applied to the part model. The heat input for the layer hatch model of the scan island is approximated by a cuboid heat source r_{ext}^c which is calibrated by using the aforementioned determined melt pool dimensions d_s and d_m and process parameters of the single melt line. This heat source is exposed to the top layer of the scan island (cf., Figure 2, middle), following a trajectory of, for example, serpentine lines. Due to the cuboid heat source, a larger element size can now be used to save computation time. In addition, only a temperature-dependent material model calibrated with the help of the results of the laser heat source model is used.

Only a mechanical simulation, that is, thermomechanical coupling as well as further direct temperature influences are neglected, with an elasto-plastic material model is used for the part model to reduce the computing time. The determined inherent strains ϵ^{inh} are applied as an external load to the complete part simulation, where the frequently used benchmark structure of a cantilever beam or any other arbitrary part can be considered. By means of the part simulation, the final eigenstresses and warpage are determined. This approach is illustrated in Figure 2, right side. The simplification is considered appropriate for the SLM process, as each melt line undergoes a similar thermomechanical history. This also results in so-called global models where complete layers are thermally loaded, see for example [18, 29, 42]. However, the overall used scan pattern of the final component can still be taken into account with the help of the multiscale framework, that is, by rotating the corresponding inherent strain tensor for the respective sections. Therefore, the previously determined inherent strain tensor can be used to model various complete units with different corresponding scan patterns, as long as the same process parameters are used. In general, this ansatz enables the efficient optimization and reduction of the final residual stresses and the deformation of the part.

Altogether, this multiscale ansatz allows to establish a simulation approach where all significant details of the SLM process are included. A comparison of the different levels, respectively models, in the multiscale framework is summarized in Table 1. In this contribution, the focus will be placed on the simulation of the single melt line and the scan island due to the fact that the core elements of modeling are included therein. The calculations of the complete part are—albeit important and interesting—not considered here, but will be the focus of future work.

Remark 1. In view of multiscale modeling frameworks for AM processes, the terms microscale, mesoscale, and macroscale are also used to indicate different model levels. Thereby, these denominations are used according to the level of analysis, see, for example, [3, 14, 16, 17, 21, 24, 40], which is in contrast to the understanding of the denomination micro, meso and macro in the context of, for example, classic solid state physics. The microscale then refers to the modeling and simulation of a single melt line, the mesoscale addresses the scan island, and the macroscale deals with the complete part. It is remarked that a clear scale separation, which is required in, for example, standard homogenization schemes, is not given in this context, compare Table 1. In order to avoid any misunderstanding and confusion of denominations used in different communities, the terms micro, meso, and macro are not used in a multiscale context in the present work, but direct reference to the respective level of analysis is made.

2.1 | Thermomechanical balance equations

As already mentioned, the simulations of the single melt line and the scan island are based on a thermomechanically coupled FE analysis. Thus, the thermomechanical balance equations shall be introduced in the following. For now, the small strain theory is assumed to be appropriate, so that the linearized strain measure

$$\boldsymbol{\varepsilon} := \frac{1}{2} [\nabla \mathbf{u} + (\nabla \mathbf{u})^t] \quad (1)$$

is used which is based on the displacement field \mathbf{u} . The total strains

$$\boldsymbol{\varepsilon} = \boldsymbol{\varepsilon}^{\text{el}} + \boldsymbol{\varepsilon}^{\text{inel}} \quad (2)$$

can be additively decomposed into an elastic part $\boldsymbol{\varepsilon}^{\text{el}}$ and an inelastic part $\boldsymbol{\varepsilon}^{\text{inel}}$, where the latter reflects the combination of various inelastic and thermal strain contributions to be specified later. In a standard manner, the (quasi-static) balance of linear momentum and the energy equation can be introduced as follows,

$$\mathbf{0} = \nabla \cdot \boldsymbol{\sigma} + \mathbf{b}, \quad (3)$$

$$0 = -\nabla \cdot \mathbf{q} + r_{\text{ext}} + \boldsymbol{\sigma} : \dot{\boldsymbol{\varepsilon}} - \rho \dot{e}, \quad (4)$$

where $\boldsymbol{\sigma}$ denotes the stress tensor, \mathbf{b} refers to body forces, \mathbf{q} is the heat flux vector, ρ represents the mass density, e describes the specific internal energy, and r_{ext} symbolizes the external heat sources. The notation $\dot{\bullet}$ denotes the time derivative of the quantity \bullet . The body forces in (3) are assumed to be negligible hereafter, such that $\mathbf{b} \equiv \mathbf{0}$. The energy equation (4) can be further specified applying the Coleman–Noll procedure, compare [6], such that

$$0 = -\nabla \cdot \mathbf{q} + r^* - \rho c \dot{\theta}, \quad (5)$$

where the contribution r^* summarizes all effective heat sources of the model, c denotes the specific heat capacity and where θ refers to the absolute temperature. The effective heat sources can be split into $r^* = r_{\text{mech}} + r_{\text{ext}}$, where r_{mech} determines the volumetric heat generation caused by mechanical working of the material. The aforementioned quantity is defined as

$$r_{\text{mech}} = D_{\text{mech}} + \theta \partial_{\theta} [\boldsymbol{\sigma} : \dot{\boldsymbol{\varepsilon}} - D_{\text{mech}}], \quad (6)$$

where D_{mech} refers to the mechanical dissipation of the material.

For the following framework, a Helmholtz free energy $\Psi(\boldsymbol{\varepsilon}, \theta, \mathcal{V})$ shall be introduced for a thermomechanical consistent framework, where \mathcal{V} refers to all internal variables. With this information at hand, the total stresses are defined as

$$\boldsymbol{\sigma} = \rho \frac{\partial \Psi}{\partial \boldsymbol{\varepsilon}}, \quad (7)$$

whereas the mechanical dissipation can be determined by

$$D_{\text{mech}} = \mathcal{F} \bullet \dot{\mathcal{V}} \geq 0. \quad (8)$$

Within (8), \mathcal{F} denotes the generalized driving force of the respective internal variable \mathcal{V} and can be further specified as $\mathcal{F} = -\rho \partial_{\mathcal{V}} \Psi$.

2.2 | Heat source model—Single melt line

A thermomechanical heat source model is used to examine the melting and solidification process of the single melt line in detail. As the results of the single melt line are relevant for both other modeling levels and therefore influence the results, an elaborated and physically motivated material model has to be implemented to take into account the various physical processes. Thus, a complex phase transformation algorithm is incorporated to define the mechanical material model of the three phases, namely, the powder, the molten, and the resolidified material. In addition, a volumetric Goldak heat source is used to model the laser beam, where the geometric parameters can be calibrated via experiments. These two modeling assumptions will be described in the following sections. Overall, the simulation has to be conducted once for each of the material and laser parameters. It can then be reused to define different scan island simulations of the layer hatch model. With the single melt line simulation results of the heat source model, both melting and resolidifying temperature are identified for the temperature dependent material model of the layer hatch model. In addition, the parameters of the cuboid heat source of the layer hatch model are determined by using the results of the heat source model.

2.2.1 | Phase transformation approach

In this section, the phase transformation approach used for the SLM process shall be introduced based on the framework presented in [28], which enhances the model introduced in [4], and the references cited therein. By means of this method, a model based on energy densities, rather than on enforcing a phase transition purely by the melting temperature, see, for example, [11, 21, 43], is used for the heat source model. Within these phase transformation models, a homogenization ansatz is applied, where the volume fractions and the volume averaged specific energy density are defined via

$$\xi_i := \frac{dV_i}{dV_0} \quad \text{and} \quad \bar{\psi} := \sum_{i=1}^{n_{\text{ph}}} \xi_i \psi_i, \quad (9)$$

respectively. Thereby, dV_0 represents the (infinitesimal) reference volume, dV_i denotes the volume of the respective phase, ψ_i refers to the volume specific energy of the respective phase, and n_{ph} corresponds to the total number of phases. In addition, mass fractions ζ_i and the averaged mass specific energy $\bar{\Psi}$ can be defined by analogy with (9), where the relation $\psi_i = \rho_i \Psi_i$ between the volume and mass specific energy densities holds. The mass fractions can now be defined and rewritten as

$$\zeta_i := \frac{dm_i}{dm_0} = \frac{\rho_i dV_i}{dm_0} = \frac{\rho_i \xi_i dV_0}{dm_0}, \quad (10)$$

where dm_0 defines the (infinitesimal) initial mass and where dm_i represents the current mass of the corresponding phase. The mass fractions are constrained to reside within the admissible region

$$0 \leq \zeta_i \leq 1 \quad \text{and} \quad \sum_i^{n_{\text{ph}}} \zeta_i = 1. \quad (11)$$

This way, the mass is the conserved quantity, that is, $\sum_i^{n_{\text{ph}}} \zeta_i = 1$. In addition, the averaged mass specific energy $\bar{\Psi}$ is introduced as

$$\bar{\Psi} := \sum_{i=1}^{n_{\text{ph}}} \zeta_i \Psi_i = \frac{dV_0}{dm_0} \sum_{i=1}^{n_{\text{ph}}} \xi_i \psi_i, \quad (12)$$

where the relation (10) is already employed. Furthermore, the compatibility condition

$$\mathbf{r}^{\varepsilon} := \boldsymbol{\varepsilon} - \sum_{i=1}^{n_{\text{ph}}} \zeta_i \boldsymbol{\varepsilon}_i = \mathbf{0} \quad (13)$$

is used which define admissible strain states $\boldsymbol{\varepsilon}_i$ within the respective phase.

For the SLM process, three phases—representing the powder, molten pool, and resolidified material—are used within the framework such that $n_{\text{ph}} = 3$. Each of these different material states is represented by an energy density ψ_{\bullet} , where $\bullet = \{\text{pow}, \text{mel}, \text{sol}\}$, corresponding to the powder, molten, and solid material, respectively. Therefore, the explicit averaged energy density employed for the framework at hand is given by

$$\bar{\Psi} = \frac{dV_0}{dm_0} \left[\xi_{\text{pow}} \psi_{\text{pow}}(\boldsymbol{\varepsilon}_{\text{pow}}, \theta, \mathcal{V}) + \xi_{\text{mel}} \psi_{\text{mel}}(\boldsymbol{\varepsilon}_{\text{mel}}, \theta, \mathcal{V}) + \xi_{\text{sol}} \psi_{\text{sol}}(\boldsymbol{\varepsilon}_{\text{sol}}, \theta, \mathcal{V}) \right], \quad (14)$$

where the aforementioned state variable \mathcal{V} includes the mass fractions but is not restricted to these, so that $\mathcal{V} = \{\zeta_{\text{pow}}, \zeta_{\text{mel}}, \zeta_{\text{sol}}, \mathcal{I}\}$. The newly introduced quantity \mathcal{I} symbolizes further, at this point still unspecified, internal variables. The specific energy densities for these three phases will be defined in Section 2.2.2. The effective energy density has to be determined based on a constrained minimization problem with respect to feasible mass fractions and compatible strains in terms of

$$\mathcal{A} = \{0 \leq \zeta_{\bullet} \leq 1, \quad \zeta_{\text{pow}} + \zeta_{\text{mel}} + \zeta_{\text{sol}} = 1, \quad \dot{\zeta}_{\text{pow}} \leq 0\}, \quad (15)$$

$$\mathcal{E} = \{\zeta_{\text{pow}} \boldsymbol{\varepsilon}_{\text{pow}} + \zeta_{\text{mel}} \boldsymbol{\varepsilon}_{\text{mel}} + \zeta_{\text{sol}} \boldsymbol{\varepsilon}_{\text{sol}} = \boldsymbol{\varepsilon}\}. \quad (16)$$

The admissible range of mass fractions in (15) has been expanded by the physical constraint $\dot{\zeta}_{\text{pow}} \leq 0$, as the melting of powder is nonreversible. This minimization leads to the so-called convexification of $\bar{\Psi}$, that is,

$$\text{C}\bar{\Psi} := \inf_{\zeta_{\bullet} \in \mathcal{A}} \inf_{\boldsymbol{\varepsilon}_{\bullet} \in \mathcal{E}} \bar{\Psi}, \quad (17)$$

where $\text{C}\bar{\Psi}$ is also known as the convex hull of the energy densities Ψ_{\bullet} .

In the following, the determination of the optimal strain distribution and the calculation of the overall stress shall be discussed briefly. For a more detailed discussion of the phase transformation approach and the calculation of the aforementioned quantities, the interested reader is referred to [28]. Considering (16), the equality constraint can be incorporated into the minimization problem with the help of a Lagrangian

$$\mathcal{L} = \bar{\Psi} + \boldsymbol{\lambda} : \mathbf{r}^{\varepsilon}, \quad (18)$$

where the Lagrange multipliers are summarized in $\boldsymbol{\lambda}$. It is assumed that the different strain states $\boldsymbol{\varepsilon}_i$ minimize (18). Consequently, the necessary conditions for the minimization are specified as

$$\partial_{\boldsymbol{\varepsilon}_{\text{pow}}} \mathcal{L} = \mathbf{0}, \quad \partial_{\boldsymbol{\varepsilon}_{\text{mel}}} \mathcal{L} = \mathbf{0}, \quad \partial_{\boldsymbol{\varepsilon}_{\text{sol}}} \mathcal{L} = \mathbf{0}. \quad (19)$$

With this information at hand, an analytical expression for the Lagrange multipliers and the optimal strains of each phase can be derived. The determination of the mass fractions and all other state variables \mathcal{V} will be considered next in Section 2.2.2. Altogether, the overall stress can then be calculated corresponding to (7) via

$$\boldsymbol{\sigma} = \frac{\partial \bar{\Psi}}{\partial \boldsymbol{\varepsilon}}. \quad (20)$$

2.2.2 | Constitutive framework

All phases are modeled as a solid continuum, where an additively decomposed energy density is chosen. This energy density can be split into a mechanical and a caloric contribution taking into account the temperature dependence of the

material model. The specific energy density of the respective phases is defined as follows,

$$\psi_{\text{pow}} := \frac{1}{2} \boldsymbol{\varepsilon}_{\text{pow}} : \mathbf{E}_{\text{pow}} : \boldsymbol{\varepsilon}_{\text{pow}} - c_{\text{pow}} \theta \ln(\theta) + L_{\text{pow}} \frac{\theta - \theta_{\text{pow}}^{\text{ref}}}{\theta_{\text{pow}}^{\text{ref}}}, \quad (21)$$

$$\psi_{\text{mel}} := \frac{1}{2} [\boldsymbol{\varepsilon}_{\text{mel}} - \boldsymbol{\varepsilon}_{\text{mel}}^{\text{inel}}] : \mathbf{E}_{\text{mel}} : [\boldsymbol{\varepsilon}_{\text{mel}} - \boldsymbol{\varepsilon}_{\text{mel}}^{\text{inel}}] - c_{\text{mel}} \theta \ln(\theta), \quad (22)$$

$$\psi_{\text{sol}} := \frac{1}{2} [\boldsymbol{\varepsilon}_{\text{sol}} - \boldsymbol{\varepsilon}_{\text{sol}}^{\text{inel}}] : \mathbf{E}_{\text{sol}} : [\boldsymbol{\varepsilon}_{\text{sol}} - \boldsymbol{\varepsilon}_{\text{sol}}^{\text{inel}}] + \frac{H_{\text{sol}}}{2} [k_{\text{sol}}^{\text{hard}}]^2 - c_{\text{sol}} \theta \ln(\theta) + L_{\text{sol}} \frac{\theta - \theta_{\text{sol}}^{\text{ref}}}{\theta_{\text{sol}}^{\text{ref}}}, \quad (23)$$

representing the powder, the molten pool, and the resolidified material, respectively. Thereby, $\boldsymbol{\varepsilon}_{\bullet}^{\text{inel}}$ denotes the inelastic strains, \mathbf{E}_{\bullet} refers to the fourth-order elasticity tensor, c_{\bullet} is the weighted heat capacity, and L_{\bullet} represents the weighted latent heat at the reference temperature $\theta_{\bullet}^{\text{ref}}$ of the respective phase \bullet . The ansatz for the caloric heat contribution, which is a function of temperature, heat capacity, and latent heat, is adopted from [10]. Here, the latent heat refers to the remaining temperature change after an adiabatic transformation cycle and is not directly related to the change of entropy. In addition, the parameters H_{sol} and $k_{\text{sol}}^{\text{hard}}$ define the isotropic hardening of the solid phase. This is assumed to be appropriate as noncyclic mechanical loading is present.

The powder is assumed to be the parent phase which behaves purely elastic. Thus, no inelastic strains $\boldsymbol{\varepsilon}_{\text{pow}}^{\text{inel}}$, and also no transformation strains $\boldsymbol{\varepsilon}_{\text{pow}}^{\text{trans}}$, are present. For the molten phase, a transformation strain $\boldsymbol{\varepsilon}_{\text{mel}}^{\text{trans}}$ is incorporated to include the volume change of the material due to the different mass densities of the powder and the molten phase. In addition, a viscoelastic strain contribution $\boldsymbol{\varepsilon}_{\text{mel}}^{\text{ve}}$ is used to model the fluid-like behavior of the molten pool. Altogether, the inelastic strains of the molten phase can be additively composed, that is,

$$\boldsymbol{\varepsilon}_{\text{mel}}^{\text{inel}} = \boldsymbol{\varepsilon}_{\text{mel}}^{\text{trans}} + \boldsymbol{\varepsilon}_{\text{mel}}^{\text{ve}}. \quad (24)$$

For the resolidified phase, a thermal $\boldsymbol{\varepsilon}_{\text{sol}}^{\text{th}}$ and a viscoplastic $\boldsymbol{\varepsilon}_{\text{sol}}^{\text{vp}}$ strain contribution are present to take into account the high strains arising from the cooling of the material. In addition, a transformation strain $\boldsymbol{\varepsilon}_{\text{sol}}^{\text{trans}}$ is, respectively, added to the solid phase, following the same argumentation as for the molten phase. Therefore, the inelastic strains of the solid phase are defined as

$$\boldsymbol{\varepsilon}_{\text{sol}}^{\text{inel}} = \boldsymbol{\varepsilon}_{\text{sol}}^{\text{trans}} + \boldsymbol{\varepsilon}_{\text{sol}}^{\text{vp}} + \boldsymbol{\varepsilon}_{\text{sol}}^{\text{th}}. \quad (25)$$

The inelastic strains will be specified in what follows and the determination of the volume fractions will subsequently be discussed.

First, the transformation strains of the molten and resolidified phase can be directly determined by previously introduced material parameters. The volume change of the material can be defined via the current volume dV_{\bullet} and the initial volume dV_0 as $dV_{\bullet} = [1 + \text{tr}(\boldsymbol{\varepsilon}_{\bullet}^{\text{trans}})] dV_0$. With the help of the correlation $dm_{\bullet} = \rho_{\bullet} dV_{\bullet}$ and the assumption of a purely volumetric transformation, the transformation strains are defined as

$$\boldsymbol{\varepsilon}_{\bullet}^{\text{trans}} := \frac{1}{3} \left[\frac{\rho_0}{\rho_{\bullet}} - 1 \right] \mathbf{I}, \quad (26)$$

where \mathbf{I} refers to the second order identity tensor and the initial mass density is denoted by ρ_0 . For this case, ρ_0 corresponds to the density of the powder phase ρ_{pow} .

For the heat expansion model, a standard linear relation is assumed for the thermal strains in the resolidified phase, that is,

$$\boldsymbol{\varepsilon}_{\text{sol}}^{\text{th}} := \alpha_{\text{sol}} [\theta - \theta_{\text{ref}}] \mathbf{I}, \quad (27)$$

where α_{sol} denotes the isotropic heat expansion coefficient and where θ^{ref} corresponds to the reference temperature of the material. Special attention has to be paid to the used reference temperature, as only the cooling (and thus shrinkage) of the material is taken into account for the heat source model and as no previous heating (and thus expansion) is considered. This also motivates the inclusion of heat expansion within the inelastic strains in (25). In this contribution, no further direct thermomechanical coupling except the thermal strains is included in (23).

The viscous strains are defined via rate-dependent evolution equations. For the molten phase, a viscoelastic strain $\epsilon_{\text{mel}}^{\text{ve}}$ with the viscosity related material constant $\eta_{\text{mel}}^{\text{ve}}$ is used, which can be specified as

$$\dot{\epsilon}_{\text{mel}}^{\text{ve}} := \frac{1}{\eta_{\text{mel}}^{\text{ve}}} \mathcal{F}_{\text{loc}}^{\text{ve}} = \frac{1}{\eta_{\text{mel}}^{\text{ve}}} \sigma. \quad (28)$$

The local driving force $\mathcal{F}_{\text{loc}}^{\text{ve}}$ only takes into account the feasible region of the molten phase, in contrast to the general driving force \mathcal{F}^{ve} , which is a value averaged over the complete domain containing all different phases due to the homogenization approach. For the special case at hand, the local driving force equals the overall stresses as defined in (20). For the solid phase, a viscoplastic material behavior is chosen instead of taking a purely plastic approach. On the one hand, a creep behavior can be observed for metals at high temperatures, which justifies the usage of viscoplasticity for the solid phase, as the temperatures are elevated directly after the phase transformation. On the other hand, a viscous approach regularizes and stabilizes the framework, such that from a computational viewpoint larger time steps are possible compared to using rate-independent plasticity, see for example [36]. The rate-dependent evolution of the viscoplastic strains $\epsilon_{\text{sol}}^{\text{vp}}$, as well as of the quantity $k_{\text{sol}}^{\text{hard}}$ which is related to isotropic hardening can be defined with the help of the yield function Φ and the Lagrange multiplier $\Delta\lambda := \Delta t \langle \Phi \rangle / \eta_{\text{sol}}^{\text{vp}}$, where Δt refers to the time increment and where $\eta_{\text{sol}}^{\text{vp}}$ corresponds to the viscosity related material constant of the solid phase, such that

$$\dot{\epsilon}_{\text{sol}}^{\text{vp}} := \Delta\lambda \frac{\partial \Phi}{\partial \mathcal{F}_{\text{loc}}^{\text{vp}}} = \frac{\langle \Phi \rangle}{\eta_{\text{sol}}^{\text{vp}}} \frac{\partial \Phi}{\partial \mathcal{F}_{\text{loc}}^{\text{vp}}}, \quad (29)$$

$$\dot{k}_{\text{sol}}^{\text{hard}} := \Delta\lambda \frac{\partial \Phi}{\partial \kappa_{\text{loc}}} = \frac{\langle \Phi \rangle}{\eta_{\text{sol}}^{\text{vp}}} \frac{\partial \Phi}{\partial \kappa_{\text{loc}}}. \quad (30)$$

Here, $\langle \bullet \rangle$ denotes the ramp function of the quantity \bullet defined as $\langle \bullet \rangle := [\bullet + |\bullet|]/2$. The quantities $\mathcal{F}_{\text{loc}}^{\text{vp}}$ and κ_{loc} correspond to the respective local driving forces. The ansatz used in (29) is also referred to as Perzyna-type viscoplasticity. For the material model at hand, a standard isotropic yield function of the type

$$\Phi := \left\| \mathcal{F}_{\text{loc,dev}}^{\text{vp}} \right\| - \sqrt{\frac{2}{3}} \left[\sigma_{\text{sol}}^{\text{y}} - \kappa_{\text{loc}} \right] = \left\| \sigma_{\text{dev}} \right\| - \sqrt{\frac{2}{3}} \left[\sigma_{\text{sol}}^{\text{y}} + \frac{\xi_{\text{sol}}}{\zeta_{\text{sol}}} H_{\text{sol}} k_{\text{sol}}^{\text{hard}} \right] \quad (31)$$

is chosen, where $\sigma_{\text{sol}}^{\text{y}}$ refers to the (constant) yield stress, H_{sol} is the hardening modulus, and $k_{\text{sol}}^{\text{hard}}$ denotes the equivalent plastic strain due to isotropic hardening of the solid phase. The abbreviation $\bullet_{\text{dev}} := \bullet - \text{tr}(\bullet)/3 \mathbf{I}$ defines the deviator of the second order tensor \bullet .

From a computational viewpoint, it is beneficial to use volume fractions as the degree of freedom, even though (14) with the feasible domain (15) is defined based on mass fractions. Volume fractions enable the use of the averaged specific volume energy density, which is also taken into account for the calculation of the overall stress and for the evolution equations of the viscous strains. With this reformulation at hand, the density of the different phases is no longer explicitly included. However, the inequality conditions r_{\bullet} still regard the physically sound region of the mass fractions ζ_{\bullet} as introduced in (15), such that

$$r_{\text{mel}} = -\zeta_{\text{mel}} \leq 0, \quad (32)$$

$$r_{\text{sol}} = -\zeta_{\text{sol}} \leq 0, \quad (33)$$

$$r_{\text{pow}} = -1 + \zeta_{\text{mel}} + \zeta_{\text{sol}} \leq 0, \quad (34)$$

$$r_{\Delta} = \dot{\zeta}_{\text{pow}} \leq 0, \quad (35)$$

have to be fulfilled. For each inequality constraint, a respective consistency parameter Γ_{\bullet} can be introduced. It is sufficient to define two evolution equations, for example, for ξ_{mel} and ξ_{sol} , as the third quantity can be computed with the help of the equality relation $\sum_i^{n_{\text{ph}}} \zeta_i = 1$. With this information at hand, the evolution equations for the two volume fractions are determined by

$$\frac{dV_0}{dm_0} \frac{\partial \bar{\psi}}{\partial \xi_{\text{mel}}^{\xi}} + \eta^{\xi} \dot{\xi}_{\text{mel}} + \frac{\rho_{\text{mel}}}{\rho_{\text{pow}}} \eta^{\xi} \dot{\xi}_{\text{pow}} = -\Gamma_{\text{mel}} \partial_{\xi_{\text{mel}}} r_{\text{mel}} - \Gamma_{\text{pow}} \partial_{\xi_{\text{mel}}} r_{\text{pow}} - \Gamma_{\Delta} \partial_{\xi_{\text{mel}}} r_{\Delta}, \quad (36)$$

$$\frac{dV_0}{dm_0} \frac{\partial \bar{\psi}}{\partial \xi_{\text{sol}}^{\xi}} + \eta^{\xi} \dot{\xi}_{\text{sol}} + \frac{\rho_{\text{sol}}}{\rho_{\text{pow}}} \eta^{\xi} \dot{\xi}_{\text{pow}} = -\Gamma_{\text{sol}} \partial_{\xi_{\text{sol}}} r_{\text{sol}} - \Gamma_{\text{pow}} \partial_{\xi_{\text{sol}}} r_{\text{pow}} - \Gamma_{\Delta} \partial_{\xi_{\text{sol}}} r_{\Delta}, \quad (37)$$

where the inequality conditions are considered and where a dissipative behavior of the phase transformation itself is regarded by the contribution η^{ξ} and the corresponding rate of the volume fraction. With this dissipative quantity η^{ξ} , the temperature range in which the phase transformation occurs can be influenced. A more detailed discussion on the evolution equations and the implementation of the local algorithm is given in [28].

Altogether, one can summarize the model specific internal state variables $\mathcal{V} = \{\epsilon_{\text{mel}}^{\text{ve}}, \epsilon_{\text{sol}}^{\text{vp}}, k_{\text{sol}}^{\text{hard}}, \xi_{\text{mel}}, \xi_{\text{sol}}\}$, the evolution equations of which have been previously defined. Consequently, the mechanical dissipation introduced in (6) can now be specified for the underlying material model to

$$D_{\text{mech}} = - \frac{\partial \bar{\psi}}{\partial \xi_{\text{mel}}^{\xi}} \dot{\xi}_{\text{mel}} - \frac{\partial \bar{\psi}}{\partial \xi_{\text{sol}}^{\xi}} \dot{\xi}_{\text{sol}} + \mathcal{F}^{\text{ve}} : \dot{\epsilon}_{\text{mel}}^{\text{ve}} + \mathcal{F}^{\text{vp}} : \dot{\epsilon}_{\text{sol}}^{\text{vp}} + \kappa \dot{k}_{\text{sol}}^{\text{hard}}. \quad (38)$$

One key advantage of the present modeling framework is exemplified by the fact, that the process-induced inherent strains can be obtained in a straight forward way via a postprocessing. Based on the inelastic strain contributions defined above, the inherent strain tensor ϵ^{inh} is defined by

$$\epsilon^{\text{inh}} = \zeta_{\text{mel}} [\epsilon_{\text{mel}}^{\text{ve}} + \epsilon_{\text{mel}}^{\text{trans}}] + \zeta_{\text{sol}} [\epsilon_{\text{sol}}^{\text{th}} + \epsilon_{\text{sol}}^{\text{vp}} + \epsilon_{\text{sol}}^{\text{trans}}]. \quad (39)$$

2.2.3 | Volumetric heat source

A double ellipsoidal volumetric heat source introduced in [13] for welding simulations is used to model the laser beam heat input r_{ext}^G . In general, the temperature gradients related to the laser beam are not symmetric with respect to the current laser path. Thus, for the distribution in front of the laser beam r_f a different ellipsoid than for the rear dispersion r_r is chosen. The heat input is defined as

$$r_f(x'_1, x'_2, x'_3) = \frac{6\sqrt{3} \eta_{\text{ab}} P f_f}{a_f b c \pi \sqrt{\pi}} \exp\left(-3 \left[\frac{x'^2_1}{a_f^2} + \frac{x'^2_2}{b^2} + \frac{x'^2_3}{c^2} \right]\right), \quad (40)$$

$$r_r(x'_1, x'_2, x'_3) = \frac{6\sqrt{3} \eta_{\text{ab}} P f_r}{a_r b c \pi \sqrt{\pi}} \exp\left(-3 \left[\frac{x'^2_1}{a_r^2} + \frac{x'^2_2}{b^2} + \frac{x'^2_3}{c^2} \right]\right), \quad (41)$$

where the total heat input is then determined via

$$r_{\text{ext}}^G = r_r + r_f. \quad (42)$$

To model this ellipsoid, the heat fractions f_f and f_r in front and rear of the center, respectively, are determined as

$$f_f = 2 \frac{a_f}{a_f + a_r}, \quad (43)$$

$$f_r = 2 - f_f. \quad (44)$$

Furthermore, the geometrical parameters a_f, a_r, b, c affect the semi-axes of the ellipsoid as visualized in Figure 3, whereas P denotes the power of the laser beam, η_{ab} is the heat absorption coefficient and x'_1, x'_2, x'_3 refer to the moving coordinate system. The coordinates $x'_i = 0$ (with $i = 1, 2, 3$) define the center of the laser beam. With the help of the coordinate x'_1 , the laser beam movement in x_1 -direction can be defined based on the laser velocity \bar{v}^{lsr} , time t , and initial position x_{01} of the laser beam, such that $x'_1 = x_1 - \bar{v}^{\text{lsr}} t - x_{01}$ is valid for the single melt track considered here. Furthermore, the relations $x'_2 = x_2$ and $x'_3 = x_3$ apply for this case, as the laser beam moves only along the x_1 -direction.

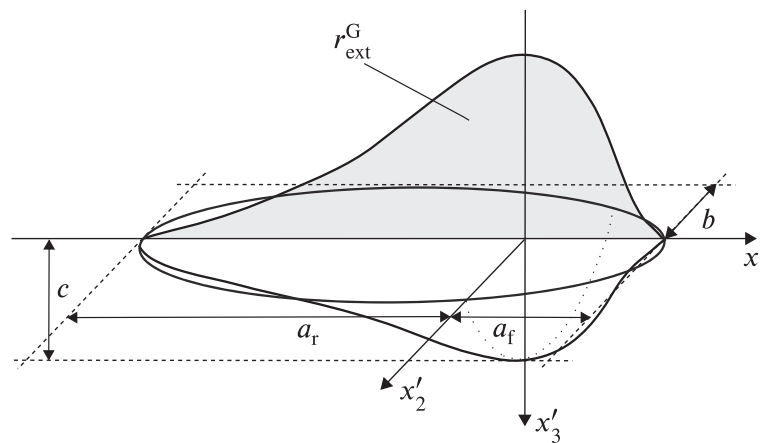


FIGURE 3 Schematic view of Goldak's ellipsoidal double well volumetric heat source

2.3 | Layer hatch model—Scan island

With the help of the layer hatch model, the scan pattern of one scan island can be analyzed. A standard size of a scan island simulation is between 1 and 5 mm, compare [7, 17] and [2, 23, 39], where the effect of different island sizes and scan strategies is investigated experimentally. A complete layer is made of continuous, see, for example, [34], or multiple island scans, where adjacent layers are rotated, compare [12]. Further and more complicated scan strategies are also examined in the literature, but have so far not been established for manufacturing processes. In addition, it is possible to study different hatching distances and layer heights with the help of the layer hatch model. To minimize the computational effort of the thermomechanical model at hand, which refers to a geometrical size larger than the one of the heat source model, two simplifications are made. At first, a material model is used which solely depends on the solidification and melting temperatures of different states of the material, that is, powder, molten, and resolidified phase. Therefore, in contrast to the heat source model, no evolution equations of mass fractions have to be solved in order to determine the current phase of the process. Furthermore, a cuboid heat source is used instead of Goldak's ellipsoidal double well which is calibrated based on the simulation results of the single melt line. To reduce the overall element number in the FE analysis, the element size is chosen in accordance to the powder layer height and the hatching distance. This is the smallest possible element size, where it is still possible to simulate the scan pattern of the scan island, compare [16]. The simulation has to be conducted once for each combination of material and process parameters, as well as hatching distance and layer height, where the inherent strains can then be extracted from the simulation results. These eigenstrains are applicable for different parts with distinct scan structures in the part model.

2.3.1 | Constitutive framework

As discussed in the previous section, a simplified approach is used for the material model of the layer hatch model. To reduce the computational time for the scan island, no evolution equations for the mass fractions using a phase transformation approach (Section 2.2.1) are included, but the phase change itself is purely temperature dependent instead. This approach seems to be appropriate for the layer hatch model, as the main focus of the scan island simulation is no longer set on the micromechanical behavior of the material on a small scale, but on the overall material response and the respective inherent strains due to the scanning strategy of a larger partition. Similar approaches are used in, for example, [21, 43]. Thus, the phase transformation now solely depends on the maximum temperature θ^{\max} , the current temperature θ and the corresponding melting and solidification temperature, θ^{melt} and θ^{solid} , respectively, which will be extracted from the single melt line simulation to resemble the material behavior defined in the phase transformation model. With this information, the phase change from the initial powder to melting and solidification can be described as a whole, as illustrated in Figure 4.

Due to the chosen ansatz of the layer hatch model, some features regarding the averaged energy densities and transformation strains shall be elaborated in the following. The lower part of the scan island already consists of solid material

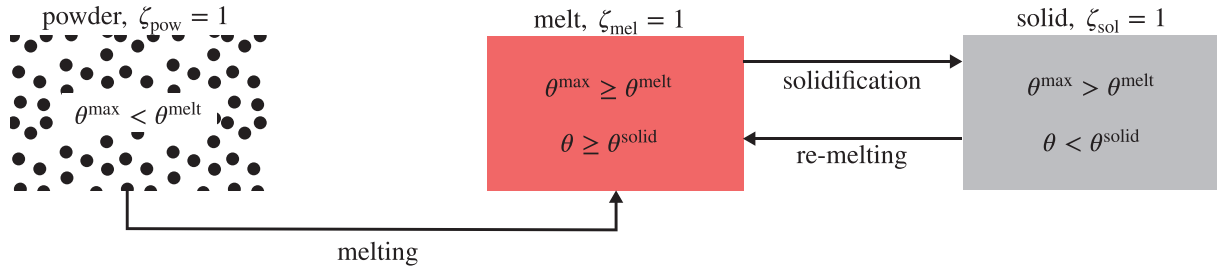


FIGURE 4 Illustration of the temperature dependent phase transformation approach used for the layer hatch model

so that the solid phase is regarded as the parent phase here. It is assumed that the lower part consists of a perfect solid without initial residual strains and stresses. The top layer, however, consists of powder, so that the powder phase is the parent phase, as also indicated in Figure 5. Therefore, a case differentiation for the two different parts of the scan island has to be taken into account. This also affects the phase transformation approach illustrated in Figure 4 due to the fact that for the lower part only the remelting and solidification process is feasible. Thus, two averaged energy densities are introduced, that is,

$$\bar{\Psi}_{\text{bottom}} = \zeta_{\text{sol}} \Psi_{\text{sol}}(\boldsymbol{\varepsilon}, \theta, \boldsymbol{\varepsilon}_{\text{sol}}^{\text{th}}, \boldsymbol{\varepsilon}_{\text{sol}}^{\text{vp}}) + \zeta_{\text{mel}} \Psi_{\text{mel}}(\boldsymbol{\varepsilon}, \theta, \boldsymbol{\varepsilon}_{\text{mel,b}}^{\text{trans}}, \boldsymbol{\varepsilon}_{\text{mel}}^{\text{ve}}), \quad (45)$$

$$\bar{\Psi}_{\text{top}} = \zeta_{\text{pow}} \Psi_{\text{pow}}(\boldsymbol{\varepsilon}, \theta) + \zeta_{\text{mel}} \Psi_{\text{mel}}(\boldsymbol{\varepsilon}, \theta, \boldsymbol{\varepsilon}_{\text{mel}}^{\text{trans}}, \boldsymbol{\varepsilon}_{\text{mel}}^{\text{ve}}) + \zeta_{\text{sol}} \Psi_{\text{sol}}(\boldsymbol{\varepsilon}, \theta, \boldsymbol{\varepsilon}_{\text{sol}}^{\text{trans}}, \boldsymbol{\varepsilon}_{\text{sol}}^{\text{th}}, \boldsymbol{\varepsilon}_{\text{sol}}^{\text{vp}}) \quad (46)$$

for the bottom and top of the scan island, respectively. As the overall material response now only comprises one phase at the same time, the phase strains $\boldsymbol{\varepsilon}_{\bullet}$ coincides with the total strain $\boldsymbol{\varepsilon}$, here. Moreover, (45) and (46) show the dependence of the particular energy density contributions on the respective inelastic strains considered. The newly introduced transformation strain $\boldsymbol{\varepsilon}_{\text{mel,b}}^{\text{trans}}$ can now be defined as

$$\boldsymbol{\varepsilon}_{\text{mel,b}}^{\text{trans}} = \frac{1}{3} \left[\frac{\rho_{\text{sol}}}{\rho_{\text{mel}}} - 1 \right] \mathbf{I}, \quad (47)$$

in analogy to (26). In addition, the volume fraction of the molten phase has to be adjusted accordingly as the solid material is now considered the reference volume and mass for the bottom material of the scan island. Corresponding to (47), the volume fraction $\xi_{\text{mel,b}} = \rho_{\text{sol}}/\rho_{\text{mel}}$ is defined, which can be derived by applying (10) and (12) to (45). All other assumptions regarding the strain contributions made in Section 2.2.2 are still valid. In other words, for the molten phase, a viscoelastic strain $\boldsymbol{\varepsilon}_{\text{mel}}^{\text{ve}}$ as introduced in (28) is present. Moreover, a thermal strain $\boldsymbol{\varepsilon}_{\text{sol}}^{\text{th}}$ as defined in (27) and a viscoplastic strain $\boldsymbol{\varepsilon}_{\text{sol}}^{\text{vp}}$ as specified in (29) and (30) exist in the solid phase. The resulting inherent strain tensor $\boldsymbol{\varepsilon}^{\text{inh}}$ of the layer hatch model is defined analogously to (39). In addition, the resulting mechanical dissipation contribution no longer depends on the evolution of the volume fractions, compare (38), but solely on the present phase and the corresponding internal variables, such that

$$D_{\text{mech}} = \begin{cases} 0, & \text{if } \zeta_{\text{pow}} = 1, \\ \mathcal{F}^{\text{ve}} : \dot{\boldsymbol{\varepsilon}}_{\text{mel}}^{\text{ve}}, & \text{if } \zeta_{\text{mel}} = 1, \\ \mathcal{F}^{\text{vp}} : \dot{\boldsymbol{\varepsilon}}_{\text{sol}}^{\text{vp}} + \kappa \dot{k}_{\text{sol}}^{\text{hard}}, & \text{if } \zeta_{\text{pow}} = 1. \end{cases} \quad (48)$$

2.3.2 | Cuboid heat source

To decrease the computational time of the layer hatch simulations, a cuboid heat source $r_{\text{ext}}^{\text{c}}$ is used to model the laser beam path of the scan island following a meandering pattern, introduced in [16, 17] as a so-called cubic heat source. A similar simplification to incorporate an equivalent body heat flux used for the layer hatch model is made in [21], whereas in [12] an approach for a likewise uniform heat source is used. For the case at hand, the size of this cuboid heat source

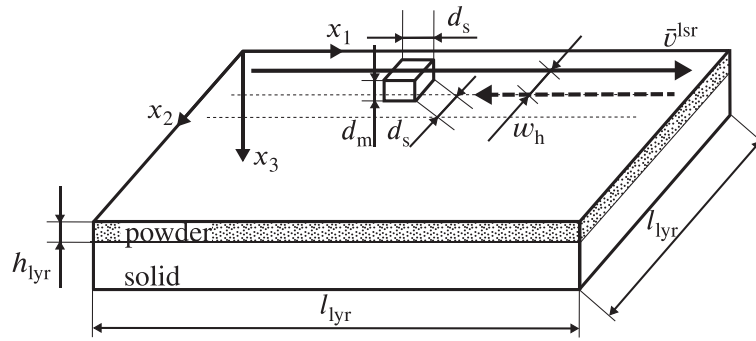


FIGURE 5 Schematic view of the cubic heat source and corresponding scan pattern

is determined by the heat source model in terms of the molten pool as described in Section 2.2. Furthermore, the scan island is spatially discretized by FEs, where each element of the regular mesh exhibits the size of the heat source. Thus, less elements are needed to resolve the layer hatch model. The newly introduced heat source can only be seen as an approximation of the laser beam heat source. It is assumed that the length of the heat source equals the width of the cuboid heat source. The edge length of the sides of the heat source is denoted by d_s , whereas d_m refers to the depth of the molten pool in the single melt line simulation. In general, the depth of the molten pool is larger than the height of the newly added layer h_{lyr} . In other words, $d_m > h_{lyr}$ has to be valid. With this information, the cuboid heat source can be defined as

$$r_{\text{ext}}^c(x'_1, x'_2, x'_3) = \begin{cases} \frac{\eta_{\text{ab}} P}{d_s^2 d_m}, & \text{if } |x'_1 - x_1| \leq \frac{d_s}{2} \wedge |x'_2 - x_2| \leq \frac{d_s}{2} \wedge h_{lyr} - x_3 \leq d_m, \\ 0, & \text{else,} \end{cases} \quad (49)$$

where P refers to the laser power and η_{ab} denotes the already introduced absorption coefficient. As a first approach, the heat source path will follow serpentine lines as used in [7, 16], which depend on the moving coordinate system x'_1, x'_2, x'_3 . For the example shown in Figure 5, the moving coordinate system is now defined via

$$x'_1 = \frac{1 - [-1]^n}{2} l_{lyr} + [-1]^n \left[\frac{d_s}{2} + \left[t - s \left\lfloor \frac{t}{s} \right\rfloor \right] \bar{v}^{\text{lsr}} \right], \quad (50)$$

$$x'_2 = \frac{d_s}{2} + n w_h, \quad (51)$$

$$x'_3 = x_3, \quad (52)$$

where the floor function $\lfloor \bullet \rfloor$ returns the largest integer value less than or equal to \bullet . Moreover, $n = \left\lfloor \frac{\bar{v}^{\text{lsr}} t}{l_{lyr} - d_s} \right\rfloor$ denotes the index of the scanned melt line, $s = \frac{l_{lyr} - d_s}{\bar{v}^{\text{lsr}}}$ is an abbreviation for the movement in x'_1 -direction, l_{lyr} refers to the length and width of the scan island and w_h represents the hatching distance. For the present case, the hatching distance equals the size of the cuboid heat source, such that $w_h = d_s$, as the scan island is not resolved in detail and the element size equals the heat source size.

3 | NUMERICAL RESULTS

In the following section, the numerical results of the single melt line and scan island simulation employing the commercial FE program Abaqus are illustrated and interpreted. As one of many appropriate materials for the SLM process, a titanium aluminum alloy $\text{Ti}_6\text{Al}_4\text{V}$ is chosen for the examples at hand. The mechanical and thermal material parameters are summarized in Table 2. So far, the hardening modulus H_{sol} and the viscous parameters $\eta^{v\bullet}$ are meaningfully selected without particular literature reference. For the viscoelastic strains in the molten phase, a high viscosity parameter

TABLE 2 Summary of the material parameters used for Ti₆Al₄V, adjusted from [25, 30, 38]

Material parameters		Powder	Melt	Solid
<i>Mechanical parameters</i>				
Density	ρ [kg/m ³]	2800	3800	4420
Poisson's ratio	ν [-]	0.33	0.45	0.33
Young's modulus	E [GPa]	1.2	2.9	88.8
Yield limit	σ^y [GPa]	-	-	0.55
Hardening modulus	H [GPa]	-	-	1
Viscosity parameter	η^v [-]	-	70	5
<i>Thermal parameters</i>				
Expansion coefficient	α [1/K]	-	-	1.1e-05
Initial temperature	θ^{ini} [K]	-	-	273.15
Heat capacity	c [J/(kg K)]	750	750	750
Conductivity	k [W/(m K)]	9.5	33.4	17.8
Latent heat	L [kJ/kg]	286	-	286
Reference temperature	θ^{ref} [K]	1873.15	-	1873.15

$\eta_{\text{mel}}^{\text{ve}} = 70$ is chosen to model the fluid-like behavior. In contrast, a lower parameter is used for the viscoplastic behavior of the solid phase, namely $\eta_{\text{sol}}^{\text{vp}} = 5$. Finally, the dissipation parameter $\eta^{\dot{\epsilon}}$ introduced for the phase change is defined as $\eta^{\dot{\epsilon}} = 0.002$. This parameter choice influences the temperature range in which the phase transformation process takes place. In the future, this parameter could be adjusted to fit experimental results. Altogether, the parameters η^{\bullet} are also used to increase the numerical stability of the FE scheme regarding the step size. With the help of the densities ρ_{\bullet} , it is possible to directly calculate the transformation strains $\epsilon_{\bullet}^{\text{trans}}$. Due to the large difference in mass densities, the volume change incorporated by the transformation strains is rather large. As the transformation strains are purely volumetric and small rotations are present, the small strain formulation is still regarded appropriate at this point. In this study, the influence of the laser power and velocity are varied to examine the effects on the melt pool size and temperature. Furthermore, the influence of the thermal behavior on the residual stresses and inherent strains shall be analyzed.

3.1 | Heat source model

The heat source model for a single melt line as introduced in Section 2.2.2 is implemented into the commercial FE software Abaqus. To incorporate the aforementioned material model, the user subroutines UMAT and UMATHT have to be used. Furthermore, the subroutine DFLUX is called during the simulation which defines the volumetric moving heat source $r_{\text{ext}}^{\text{G}}$ according to Section 2.2.3.

3.1.1 | Characteristics of heat source model

Initially, the whole domain consists of powder so that $\zeta_{\text{pow}} = 1$. Furthermore, the complete domain is preheated to $\bar{\theta} = 373.15$ K to resemble the preheating of the building chamber. During the simulation, this temperature is set constant at the bottom of body considered, whereas all other sides are assumed to be insulated, so that heat convection and radiation are neglected. The volumetric moving heat source resembling the laser beam embeds thermal energy into the part. Afterwards, the unit cools down to the temperature of the building chamber. During the whole simulation, the displacements of the bottom and the sides of the component are fixed. The domain with the corresponding Dirichlet boundary conditions on the boundaries $\partial\mathcal{B}$ is illustrated in Figure 6A, whereas the mesh and the geometric size of the domain is defined in Figure 6B. The element size is set to a characteristic length of $l_{\text{char}} = 20$ μm which approximately corresponds

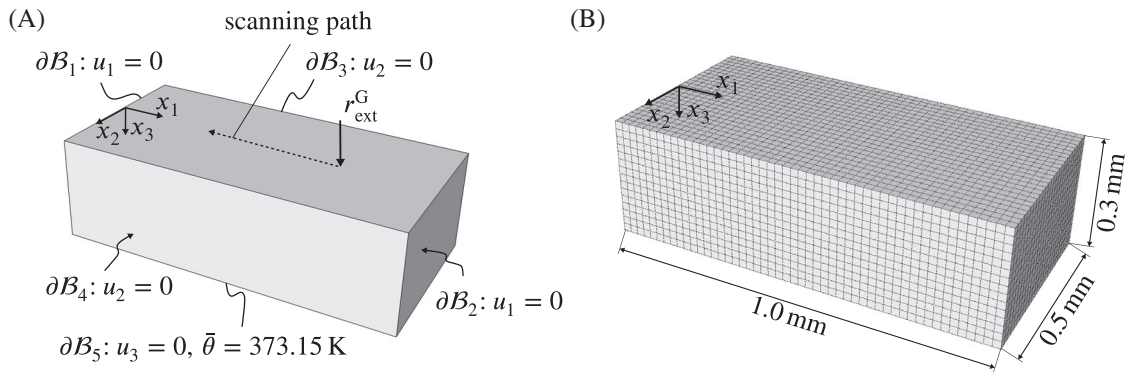


FIGURE 6 Specification of the simulation model for the heat source model of a single melt line: (A) boundary conditions and loads, (B) overall dimensions with corresponding mesh (element size equals $20 \mu\text{m}$)

to the range of the size of the powder particles, see, for example, [8]. The used element type throughout all simulations is C3D8T, an eight node thermally coupled brick element with trilinear shape functions for displacements and temperature.

The volume-distributed heat source r_{ext}^G moves along the indicated scanning path in Figure 6A. For the single melt line simulation, constant parameters of the heat source are used for the semi-axis of the ellipsoid. For now, the variables are chosen to resemble a laser beam with a focus radius of $50 \mu\text{m}$. The parameters $a_f = a_r = 50 \mu\text{m}$ and $b = 50 \mu\text{m}$ are used which corresponds to a hemispherical distribution in x_1 - and x_2 -direction, whereas the penetration depth is set to $c = 100 \mu\text{m}$. The absorption coefficient is selected as $\eta_{\text{ab}} = 0.6$. For the values of the laser power P and the laser velocity \bar{v}^{lsr} different parameter combinations are used, where the influence of $P = \{50, 100, 150\} \text{ W}$ and $\bar{v}^{\text{lsr}} = \{0.5, 1.0, 1.5\} \text{ m/s}$ is studied.

3.1.2 | Influence of parameter variation on melt pool size

First, the influence of laser power and laser velocity on the melt pool size is analyzed. Therefore, both parameters are varied to examine the effects on the thermal behavior. As it is difficult to determine the length of the melt pool in experiments, only the depth and the width of the melt pool are measured according to Figure 7B. One advantage of the phase transformation approach is the possibility to visualize the heat affected zone (HAZ) underneath the melting range which is often neglected in common approaches. Due to the evolution equations which are used for the mass fractions, it is not only distinguished between temperatures above and underneath the melting point, but the temperature history and residual strains also affect the final values of the mass fractions. The temperature profile during the simulation is exemplarily visualized in Figure 7A, where red color refers to the temperature above the standard melting point of $\text{Ti}_6\text{Al}_4\text{V}$ in literature ($\theta^{\text{ref}} = 1873.15 \text{ K}$). Overall, the maximum temperature increases drastically with growing laser power and fixed scan speed, whereas the cooling rate increases with reduced scan speed for fixed laser power. The HAZ in Figure 7B is similar to the one in the experiments, see for example [8], where a $\text{Ti}_6\text{Al}_4\text{V}$ baseplate has been used instead of working in a complete powder bed. With increasing distance from the actual melt pool, the influence on the material decreases and the solid mass fraction also reduces. Altogether, the temperature profile in Figure 7A and geometry of the melt pool region in Figure 7B resemble a bowl shape. The reduction in height, that is, in x_3 -direction, at the top layer of Figure 7A is due to the transformation strain $\epsilon_{\text{mel}}^{\text{trans}}$, whereas the larger height-wise decrease in Figure 7B stems from the additional transformation strain $\epsilon_{\text{sol}}^{\text{trans}}$ and the thermal shrinkage based on $\epsilon_{\text{sol}}^{\text{th}}$. The difference between the size of the red bowls in the aforementioned figures is further explained in Section 3.1.3.

With Figure 7B, it is possible to extract the melt pool geometry for all parameter combinations, as illustrated in Figure 8. It is visible that with an increase in laser power intensity, the width and depth of the melt pool increases, whereas both quantities decrease with increasing laser velocity. In this plot, the simulation results can be directly compared with experimental results shown in, for example, [8], where the same findings were made. Without any further parameter determination or validation, for example referring to the semi-axes of the Goldak heat source or the heat absorption coefficient, a similar behavior can be seen for the bead width of the melt pool size, see Figure 8B, whereas the depth of penetration seems to be constantly larger in our simulations than in the experimental investigations. In a next step,

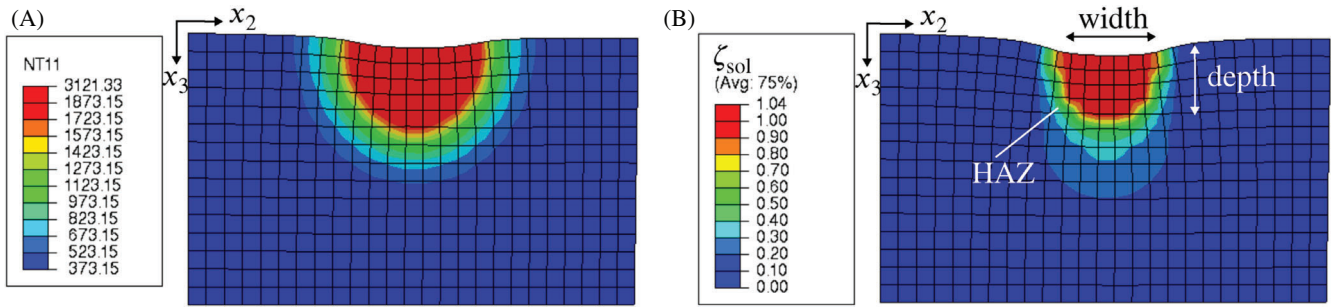


FIGURE 7 Cut at $x_1 = 0.5$ mm in the x_2 - x_3 -plane for simulation case $P = 150$ W and $\bar{v}^{\text{lsr}} = 1.0$ m/s: (A) Temperature profile θ (NT11) in [K] during the simulation, (B) solid mass fraction ζ_{sol} after cooling down, visualizing the heat affected zone and dimensions of the solidified material

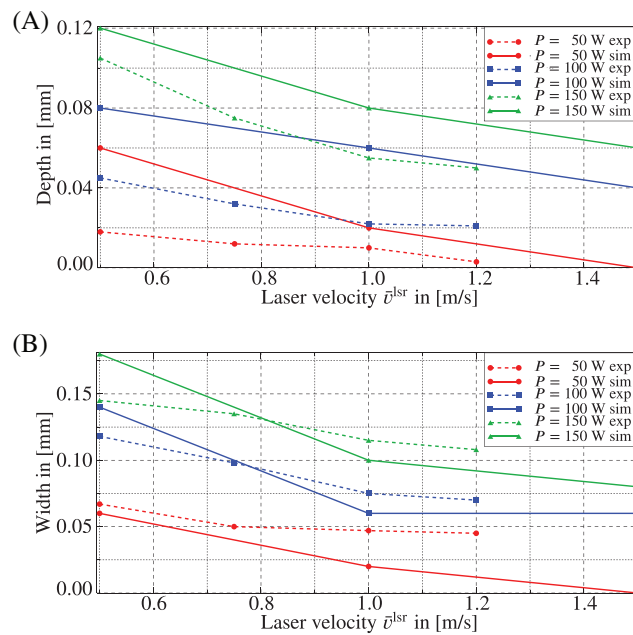


FIGURE 8 Size of melt pool in simulation based on phase transformation algorithm (solid line) compared to experimental results in [8] (dashed line): (A) Depth and (B) width of the corresponding melt pool geometry

parameter c of the Goldak heat source could therefore be adapted to fit the experimental results even better. Overall, the phase transformation algorithm is able to predict different melt pool geometries depending on the velocity and the power of the laser beam. However, with such a model it is not possible to determine effects based on porosity or balling. For such simulation results, even more detailed models of the single powder particles are necessary. It is only possible to make predictions regarding the existence of a melt pool, for example, a parameter combination of $P = 50$ W and $\bar{v}^{\text{lsr}} = 1.5$ m/s is not sufficient for a regular continuous melt pool. With the single track simulation results concerning the melt pool geometry, it is possible to extract the proper parameter combinations for the scan island simulation, where at least a melt pool width of 0.6 mm and depth of 0.6 mm are desired. The influence on the eigenstrains and stresses shall be discussed when presenting the results of the suitable layer hatch model for the scan island simulations in Section 3.2.3.

3.1.3 | Comparison of material models

Before presenting the results of the layer hatch model, the material models introduced in Sections 2.2.2 and 2.3.1 shall be compared and the melting and solidification temperature has to be determined. Therefore, the time evolution of a

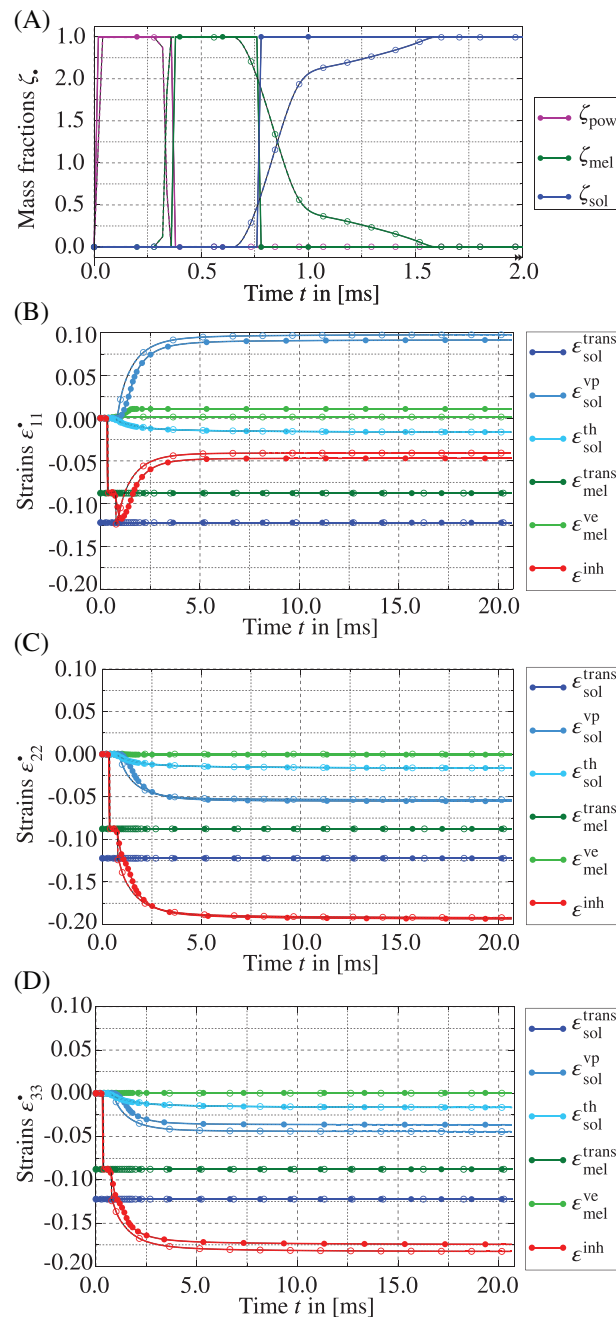


FIGURE 9 Comparison of phase transformation model (heat source approach, blank circles) and temperature dependent material model (layer hatch approach, solid circles) exemplary for simulation case $P = 100 \text{ W}$ and $v^{\text{lsr}} = 1.0 \text{ mm/s}$ for one representative element in the middle of the melt pool: (A) excerpt of development of mass fractions over time, (B–D) evolution of all strain components over time

completely molten element within the melt pool line is extracted for both simulations and visualized in Figure 9. For these results, the same model assumptions explained in Section 3.1.1 are used, only changing the material model incorporated in the subroutine UMAT. For the layer hatch model, both the melting temperature $\theta^{\text{melt}} = 1993.15 \text{ K}$ and the solidification temperature $\theta^{\text{solid}} = 1710.15 \text{ K}$ have been extracted from the results of the heat source model at a material point level. These temperatures indicate where the respective process starts in the heat source model. This also explains the different sizes of the bowl shapes in Figure 8, as a temperature of θ^{melt} is necessary for a purely molten and then solidified material point when using the phase transformation approach.

First, the mass fraction distributions are outlined in Figure 9A, where the dashed line refers to the phase transformation approach and where the solid line indicates the material behavior of the layer hatch model. Here, it can be seen how

the phase transformation model allows an evolution of the mass fractions. Especially for the solid mass fraction ζ_{sol} an extended time span is necessary for solidification, as the cooling period takes longer than heating up the material above the melting point with the laser beam. After a time span of $t = 2.0$ ms, no further development of the mass fractions is visible, as the temperature for the respective element has decreased below the melting point. In contrast, the mass fractions directly jump from zero to one when using the layer hatch approach. The normal inelastic strain contributions and the corresponding inherent strains ϵ^{inh} according to (39) are visualized in Figure 9B–D. In particular, the respective inherent strain $\epsilon_{ij}^{\text{inh}}$ can be calculated by weighting the appropriate inelastic strains with the mass fractions visualized in Figure 9A. The coordinate system at hand corresponds to the principal axes up to numerical accuracies, that is, $|\epsilon_{ij}| \ll |\epsilon_{ii}|$ (no summation with respect to i and $i \neq j$), such that the shear components are approximately zero. Therefore, only the normal components are visualized. The first drop in the inherent strains ϵ^{inh} arises due to the transformation strain of the molten phase $\epsilon_{\text{mel}}^{\text{trans}}$, whereas the second drop and the following evolution is mainly governed by the transformation strain of the resolidified material $\epsilon_{\text{sol}}^{\text{trans}}$ and the viscoplastic strain $\epsilon_{\text{sol}}^{\text{vp}}$. The influence of the viscoelastic strains of the molten phase $\epsilon_{\text{mel}}^{\text{ve}}$ is negligible as no previously present residual strains exist for the molten phase during a single melt line. Overall, high direction-dependent viscoplastic and inherent strain contributions are visible for the single melt track. A high viscoplastic tensile strain $\epsilon_{11}^{\text{vp}}$ is present in scanning direction, whereas all other strains are compressive. Especially high compressive inherent strains $\epsilon_{22}^{\text{inh}}$ and $\epsilon_{33}^{\text{inh}}$ exist transversal and vertical to the laser beam movement. The thermal strains and the transformation strains are uniformly distributed according to (27) and (26), respectively. During the evolution of the strains, larger differences can be seen in the range of $t_1 \approx 0.75$ ms to $t_2 \approx 4.0$ ms, as the different evolution of the mass fractions notably influences the respective values. However, during the following process of cooling, the discrepancy further reduces and a steady-state is reached. The final deviation at $t = 20.0$ ms, where the part has completely cooled down to $\theta^{\text{end}} \approx 393$ K, is minor compared to the absolute values of the quantities itself. All in all, the conclusion is permitted that the layer hatch model is sufficiently accurate, if only the final residual strains for completely molten and resolidified particles are relevant. However, the layer hatch model neither precisely covers the phase transformation behavior nor can display partly molten particles in the HAZ.

3.2 | Layer hatch model

The layer hatch model for the scan island simulations is also implemented into the commercial FE software Abaqus. The user subroutines UMAT and DFLUX have to be adapted according to the material behavior described in Section 2.3.1 and according to the cuboid heat flux r_{ext}^c defined in Section 2.3.2, respectively. The same subroutine UMATHT can be used for the thermal material model as well.

3.2.1 | Definition of layer hatch model

A simple model resembling a single scan island is employed for the layer hatch model, where the lower portion is initially made out of solid material, thus $\zeta_{\text{sol}} = 1$. In contrast, the powder material with $\zeta_{\text{pow}} = 1$ is assigned to the top layer as indicated in Figure 10A. The complete domain is preheated to $\bar{\theta} = 373.15$ K. During the simulation, this temperature is prescribed at the bottom of the body considered. In addition, no displacements are allowed at the bottom, while all other sides have no predefined conditions. All boundary conditions and loads are illustrated in Figure 10A. In the following, two different scan island sizes with the side length $l_{\text{lyr}} = \{3, 5\}$ mm are considered. The geometry is exemplarily shown in Figure 10B, where Δl refers to a domain of five elements of the respective simulation which are not molten by the laser beam heat source. These elements indicate the surrounding powder bed during the scanning of the scan island. This distance seems to be sufficient, as the surrounding powder has a low conductivity and Young's modulus. Thus, only a small buffer zone is necessary, see, for example, [7], where almost no temperature influence is visible on powder particles further away from the laser beam. The height of the powder layer corresponds to the height of half an element, thus $h_{\text{lyr}} = d_m/2$, whereas the hatching distance equals the element length $w_h = d_s$. As already explained in Section 2.3, the element size is chosen according to the size of the melt pool. However, sufficiently large melt pools are necessary to obtain a proper process model, so that only the material combinations defined and summarized in Table 3 are considered. Altogether, the results presented in Figure 8 directly affect the layer hatch model and simulation. Two values in Table 3 (edge height d_m for cases 4 and 5) are adapted to ensure a completely molten element because the initial energy input was not high enough to completely melt the element for these large melt pools. As the element size also influences the necessary melt line

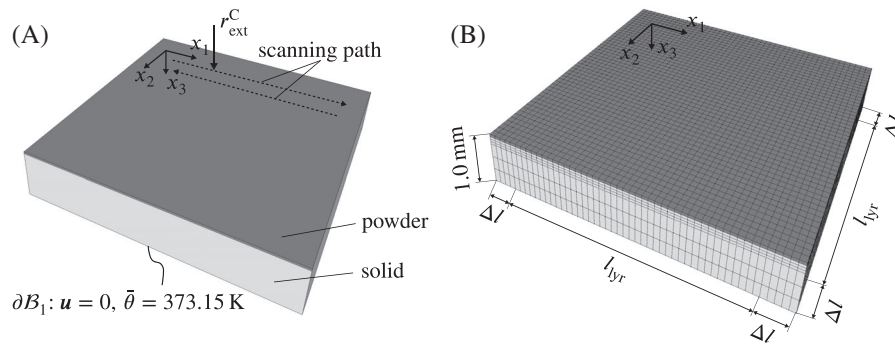


FIGURE 10 Specification of the simulation model for the layer hatch model: (A) boundary conditions and loads, (B) geometry of the scan island with corresponding mesh (element size equals melt pool size)

TABLE 3 Overview of the laser beam parameters and cuboid heat source sizes for the layer hatch model

Case	Laser power, P	Laser velocity, \bar{v}_{lsr}	Edge length, d_s	Edge height, d_m
1	50 W	0.5 m/s	0.06 mm	0.06 mm
2	100 W	0.5 m/s	0.14 mm	0.08 mm
3	100 W	1.0 m/s	0.06 mm	0.06 mm
4	150 W	0.5 m/s	0.18 mm	0.10 mm
5	150 W	1.0 m/s	0.10 mm	0.06 mm
6	150 W	1.5 m/s	0.06 mm	0.06 mm

tracks of the meandering pattern, the time period to completely melt the scan island has to be adaptively chosen according to the laser beam velocity, the element size and the size of the scan island. After having scanned the complete island in a meandering pattern with the cuboid heat source r_{ext}^c as marked in Figure 10A, an appropriate time span $t^{\text{end}} = 100$ ms is chosen so that the part can (almost) completely cool down to the initial temperature $\bar{\theta}$. The impact of these different process parameters, that is, laser power, scan speed and island size, on the layer hatch model results are presented next.

3.2.2 | Influence of parameter variation on scan island

First the influence of the melt pool seam and thus the impact of the different laser beam parameters shall be discussed. Here, especially the effect on the process time and the thermal material behavior is analyzed. An overview of the necessary scan tracks n and time periods t^{lsr} is given in Table 4 for the smaller scan island $l_{\text{lyr}} = 3$ mm. The impact on the necessary time period t^{lsr} and on the maximum average temperature θ^{avg} , that is, the maximum temperature averaged over one element, is obvious. For a low laser power and velocity, the longest time span is necessary (case 1). The process parameters of cases 4–6 create the fastest scan islands time-wise. Especially keeping in mind that each complete part consists of multiple layers with many scan islands, the time period for manufacturing each scan island considerably affects the overall process time.

The average temperature of the element during scanning varies drastically due to the element size, laser velocity, and power as summarized in Table 4. For a constant laser beam power, the temperature increases with increasing laser velocity when applying a cuboid heat source with a geometry as defined in Table 4. In contrast, the end temperature θ^{end} after cooling down for $t^{\text{end}} = 100$ ms barely differs. In Figure 11A, the temperature distribution for case 6 at the specific time frame $t^{\text{lsr}} = 29.4$ ms during the scanning period is illustrated, where a maximum temperature of $\theta^{\text{avg}} = 4308.99$ K is reached. Even though evaporation is possible above $\theta^{\text{vap}} \approx 3533$ K, it is appropriate to neglect this process in the layer hatch model as the melt pool is considered as a whole. The corresponding size of the molten pool and the already solidified

TABLE 4 Summary of scan island results for $l_{\text{yr}} = 3$ mm

Case	Scan tracks, n	Time period, t^{lsr}	Avg. temperature, θ^{avg}	End temperature, θ^{end}
1	50	294.00 ms	2616 K	430 K
3	50	147.00 ms	3225 K	455 K
2	21	117.60 ms	2055 K	426 K
6	50	98.00 ms	4309 K	467 K
4	17	97.92 ms	2477 K	440 K
5	30	87.00 ms	3373 K	444 K

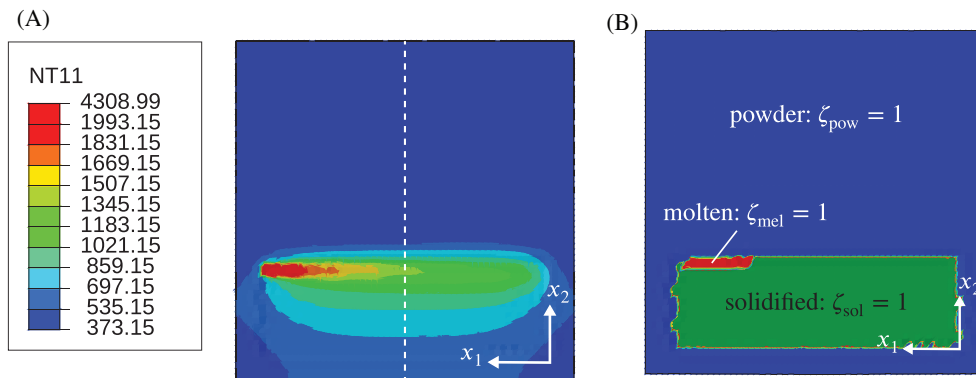


FIGURE 11 (A) Temperature θ (NT11) in [K] and (B) corresponding material state for case 6 ($P = 150$ W, $v^{\text{lsr}} = 1.5$ m/s) and $l_{\text{yr}} = 3$ mm at $t^{\text{lsr}} = 29.4$ ms

material is presented in Figure 11B. For all cases, the laser beam completely melts the powder within the inner region of $l_{\text{yr}} = 3$ mm. In addition, the solid material underneath is also partly remelted so that a compound with proper bonding between the layers is formed. In addition, adjacent elements are heated up numerous times below the melting point due to the influence of neighboring scan tracks, see again, for example, Figure 11A. Changing the layer thickness and hatching distance can further influence the magnitude of remelting of previous particles, however these parameters are limited as a sufficient bonding between layers has to exist. Furthermore, it has to be kept in mind that they also regulate the production rate during manufacturing.

Analogous temperature ranges can be reported for the larger scan island $l_{\text{yr}} = 5$ mm. However, slightly different cooling and reheating rates are present due to the distinct length of the scan track. In [20], the influence on cooling and reheating due to the length of scan vectors is discussed. Using larger scan vectors results in a slower rescanning of adjacent tracks so that more cooling occurs in between. The number of scan tracks for $l_{\text{yr}} = 5$ mm can be determined by scaling the respective results in Table 4 with $5/3$, that is, weighting the number of scan tracks with the size of the scan islands, whereas the overall time period has to be calculated with respect to the laser velocity. However, with regard to time efficiency, cases 4–6 are once again preferable.

Altogether, the thermal model of the scan island can be seen as a plausible approximation, where employing a cuboid heat source saves an enormous amount of computational time. However, using a cuboid heat source with an element size having the magnitude of the melt pool also results in some drawbacks. As the hatching distance equals the width of the melt pool, no studies on the influence of overlapping scan lines is possible, see, for example, [9]. These studies could albeit be incorporated into the heat source model. In addition, the cuboid heat source obviously no longer represents the real contour of the melt line compared to the Goldak heat source. However, only these simplifications can provide computational efficient models for large parts. In the next section, the influence of the thermal behavior and of the scan island size on the residual stress and inherent strain is examined.

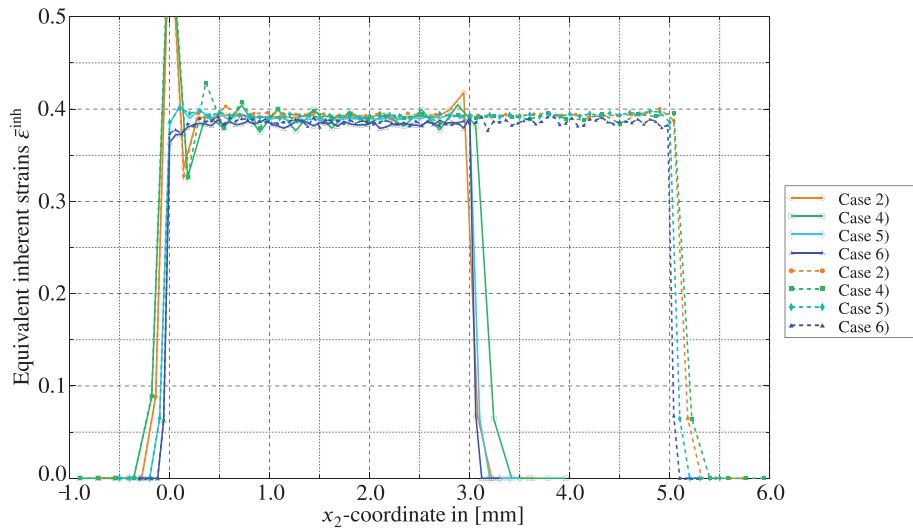


FIGURE 12 Equivalent inherent strain $\bar{\epsilon}^{\text{inh}}$ along the x_2 -direction for $l_{1\text{yr}} = 3$ mm (solid line) and $l_{1\text{yr}} = 5$ mm (dashed line) using the computational efficient cases according to Table 4

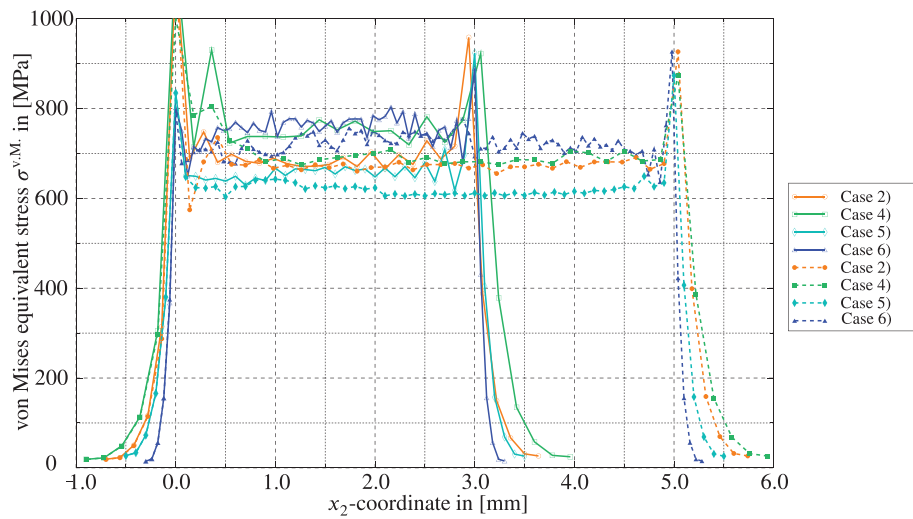


FIGURE 13 Von Mises equivalent stress $\sigma^{\text{v.M.}}$ in [MPa] along the x_2 -direction for $l_{1\text{yr}} = 3$ mm (solid line) and $l_{1\text{yr}} = 5$ mm (dashed line) using the computational efficient cases according to Table 4

3.2.3 | Final inherent strain and eigenstress distribution

In this section, the effect of the different parameters on the residual stresses and inherent strains shall be evaluated. First, the equivalent inherent strain

$$\bar{\epsilon}^{\text{inh}} = \sqrt{0.5 \left[\left[\epsilon_{11}^{\text{inh}} - \epsilon_{22}^{\text{inh}} \right]^2 + \left[\epsilon_{22}^{\text{inh}} - \epsilon_{33}^{\text{inh}} \right]^2 + \left[\epsilon_{33}^{\text{inh}} - \epsilon_{11}^{\text{inh}} \right]^2 + 6 \left[\epsilon_{12}^{\text{inh}2} + \epsilon_{13}^{\text{inh}2} + \epsilon_{23}^{\text{inh}2} \right] \right]} \quad (53)$$

is defined analogously to the von Mises equivalent stress $\sigma^{\text{v.M.}}$. Both quantities are visualized for the computational efficient cases, that is, referring to case 2 and cases 4–6, for either scan island size in Figures 12 and 13, respectively. The variables are plotted along the x_2 -coordinate, where the corresponding position x_1 and the respective path for which the values are extracted, are marked in Figure 11A.

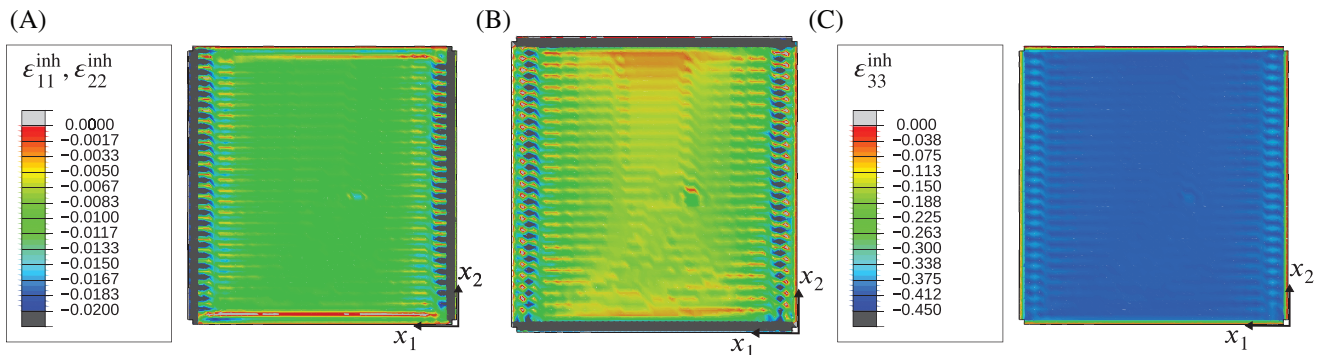


FIGURE 14 Inherent strain distribution of a single layer at the end of the simulation for case 5, that is, $P = 150 \text{ W}$, $\bar{v}^{\text{lsr}} = 1.0 \text{ m/s}$, and $l_{\text{lyr}} = 5 \text{ mm}$: (A) $\epsilon_{11}^{\text{inh}}$, (B) $\epsilon_{22}^{\text{inh}}$, and (C) $\epsilon_{33}^{\text{inh}}$

Considering Figure 12 first, the averaged inherent strains within the resolidified material in the interval $x_2 \in [0.0, 3.0]$ mm, respectively, $x_2 \in [0.0, 5.0]$ mm, are rather constant across the scan island itself. Only the inherent strains directly at the transition zone from powder to solid (especially close to $x_2 = 0.0$ mm) have to be excluded. Due to the jump-type distribution of ϵ^{inh} and the underlying (C^0 -continuous) spatial discretization, these values oscillate at the transition from powder to resolidified material. The contributions within these oscillating areas will be neglected when extracting the inherent strain tensor for the part model. This is reasonable, as the values of the inner region are (quasi) constant and predominate the contributions of the transition zone. Overall, the range of the different equivalent inherent strains in Figure 12 is quite narrow for the middle region of the resolidified material and almost independent of the underlying case. Only for the exterior values, where powder material stills exists, the inherent strains are equal to zero. However, the overall behavior differs when regarding Figure 13, where the mean value of the von Mises equivalent stresses clearly varies for the different cases. The zigzag response in Figure 12 and especially in Figure 13 is assumed to reduce when refining the mesh. However, an increasing element number is in contrast to the purpose and idea of the layer hatch model, where a computational efficient simulation is requested. Altogether, not only the inherent strain itself but also the length of the scanning vector considerably influences the residual stresses. It can be concluded that with increasing scan track length l_{lyr} the residual stresses decrease for all cases. This result coincides with the conclusions made in, for instance, [23] where 2×2 , 3×3 , 5×5 , and $7 \times 7 \text{ mm}^2$ island scanning strategies were experimentally compared for IN718. Here, the $5 \times 5 \text{ mm}^2$ scan island pattern had the lowest residual stresses while having the best mechanical properties, as cracking was present for the $2 \times 2 \text{ mm}^2$ scan island size. In [20], it is reasoned that sectors-wise scanning should be preferred for an Fe-powder mixture, compared to scanning along the x_1 - or x_2 -direction only, as the least curvature was present. However, no remarkable deviation existed for the experiments when using 2.5×2.5 and $5 \times 5 \text{ mm}^2$ island patterns. It therefore has to be examined in the future how the scanning vector influences the overall residual stresses and curvature when simulating one large layer or complete part with the extracted inherent strains.

For the present simulations, the lowest residual equivalent stress is observed for case 5 and $l_{\text{lyr}} = 5 \text{ mm}$. For this case, the respective inherent strains along the x_1 -, x_2 -, and x_3 -direction are visualized in Figure 14, respectively. Here, only the resolidified material of the newly added layer is shown. The oscillating values at the boundaries are neglected in the following discussion, as they arise due to the jump-type behavior and projection operation applied as previously mentioned. These boundaries will not be taken into account when determining an averaged inherent strain tensor for the part model. It becomes visible that all directional inherent strains are negative due to the thermal shrinkage and the transformation strains. The normal components $\epsilon_{11}^{\text{inh}}$ and $\epsilon_{22}^{\text{inh}}$ are minor compared to $\epsilon_{33}^{\text{inh}}$. Along the laser beam movement in x_1 -direction and perpendicular in x_2 -direction, almost the same inherent strain magnitude is visible. Upright, the strains are marginally higher and the distribution is not as uniform as it is for the other two directions. This is in contrast to the results in, for example, [16] for SS316L, where higher inherent strains along the scanning direction are predicted. However, similar findings are made, for example, in [5] for IN718, where a steady-state inherent strain tensor is extracted with uniform negative values for the transversal and longitudinal direction. These inherent strains are then applied to the model of the complete part. Overall, the distribution of the inherent strains for the scan island is contrary to the results of the single melt line in Figure 9. However, in comparison to a single melt line, the material cannot contract as freely due to the preceding melt lines and the solid base plate. Therefore, the distribution is more uniform on the x_1 - x_2 -plane with lower residual strains. Higher inherent strains are present in the x_3 -direction, that is, the depth of the powder layer, where

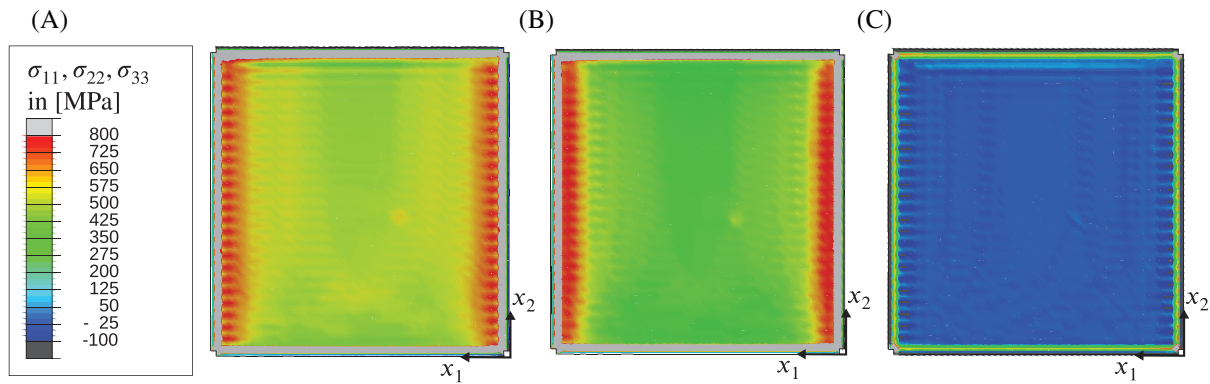


FIGURE 15 Residual stress distribution of a single layer at the end of the simulation for case 5, that is, $P = 150 \text{ W}$, $v^{\text{lsr}} = 1.0 \text{ m/s}$, and $l_{\text{lyr}} = 5 \text{ mm}$: (A) σ_{11} , (B) σ_{22} , and (C) σ_{33} in [MPa]

the shrinkage of the material caused by the transformation strains is mainly absorbed. In the literature, shear strains are oftentimes a priori neglected (for the coordinate system at hand) in the part model, compare [16, 22, 34, 35], as the influence of these strain contributions is assumed insignificant. For the current simulation, the shear components $\epsilon_{12}^{\text{inh}}$ and $\epsilon_{13}^{\text{inh}}$ are close to zero, whereas the shear component $\epsilon_{23}^{\text{inh}}$ lies within the (positive) range of $\epsilon_{11}^{\text{inh}}$ and $\epsilon_{22}^{\text{inh}}$, that is, up to $\epsilon_{23}^{\text{inh}} \approx 0.02$. Overall, the inherent strains are (quasi) constant within the not pictured layer height, that is, in x_3 -direction, as only one element is used per layer to establish a computational efficient simulation.

Altogether, rather stationary equivalent inherent strains can be extracted along the x_2 -coordinate of Figure 12, where the value of the inherent strain tensor has to be extracted carefully when applying this quantity to the part model in the future. This coincides with the findings regarding Figure 9, where the directional inherent strains are nearly uniform. This leads us to the conclusion that extracting an inherent strain tensor ϵ^{inh} , which can be applied to the complete part, is an appropriate approximation for a computational efficient model, compare, for example, [5, 16, 17, 22].

With these inherent strains, the residual stress distribution as illustrated in Figure 15 is gained. Within the inner region of the scan island, stationary residual stresses can be found. Thereby, σ_{11} and σ_{22} are positive tensile stresses, whereby the stresses in the x_1 -direction visualized in Figure 15A are superior to the ones in x_2 -direction in Figure 15B. Thus, the highest residual stresses are present along the melt line track. In x_3 -direction, negative compressive residual stresses exist, see Figure 15C. The so-called temperature gradient mechanism (TGM) is generally made responsible for the creation of stresses, see, for example, [5, 20, 42], where a bending of the body considered toward the laser beam, that is, in direction of $-x_3$, is explained by different tension and compression stresses throughout the layers. Due to the surrounding solidified material, the thermal expansion induced by the laser beam is constrained and thus nonuniform compressive stresses and strains arise. During cooling, thermal shrinkage is also restricted resulting in tensile stresses and strains. Once the manufactured part is detached from the base plate, the bending and overall deformation will become visible as a stress relaxation takes place during this process. This feature can only be observed if a complete part simulation is added to the multiscale framework causing the necessity for efficient and accurate part simulation models.

4 | CONCLUSION AND OUTLOOK

The scope of this article is to use a micromechanically motivated phase transformation approach for the heat source model of the single melt line and still to be able to predict residual stresses of realistic-sized parts in the future. To do so, a multiscale approach based on the ISM is presented. A coupled thermomechanical simulation has been introduced, differentiating between a heat source model and a layer hatch model applied to a scan island. For the single melt line simulation, a phase transformation model with a Goldak heat source is used. In contrast, the phase changes are purely temperature dependent for the material model of the layer hatch model so that a complete scan island can be efficiently simulated. The model of the scan island is capable of reproducing the residual strains and stresses of the model of the single melt line. For the layer hatch model, a cuboid heat source is used to further decrease computation time. Different sets of technological parameters (laser beam, scan velocity, island size) were considered to examine the influence on the inherent strains and residual stresses. This framework adequately predicts different melt pool geometries and reasonable

residual stresses. It is concluded that constant inherent strains can be extracted for the layer hatch model to be applied later to the simulation of a complete part. To ensure a satisfactory process efficiency, an appropriate choice regarding laser velocity and melt pool size is necessary. Based on these findings, a larger scan island is preferable.

In the future, the framework shall be extended to a part model to simulate the residual stresses and deformation of complete parts. Therefore, an averaging procedure to determine the inherent strain tensor for the corresponding set of laser parameters has to be defined. This quantity is then passed over to the mechanical FE simulation of the complete part. Especially, the heat source model needs to be calibrated with experiments to achieve reliable results. With these outcomes, it would then be possible to verify the deformation of the scan island simulations. To be able to use the phase transformation algorithm for the layer hatch material model, this framework has to be computationally optimized. However, from a micromechanical viewpoint, the material model should preferentially not be simplified for the scan island simulation of the layer hatch model. An enhancement of the evolution equations explicitly taking into account the cooling rate of the solid phase would be of particular interest. In addition, an even more complicated phase transformation model could be incorporated, where two solid phases represent the α - and β -phase of the titanium alloy. This could further improve the predicted residual stresses and deformation. Due to the rather large inelastic strains, an extension of the model to a large strain formulation may be necessary for an accurate prediction.

ACKNOWLEDGEMENTS

We would like to thank Lena Koppka for her very useful support particularly with respect to the modeling and self-written codes incorporated in the Abaqus user subroutines.

In addition, the authors gratefully acknowledge the computing time provided on the Linux HPC cluster at TU Dortmund University (LiDO3), partially funded in the course of the Large-Scale Equipment Initiative by the German Research Foundation (DFG) as project 271512359. Open Access funding enabled and organized by Projekt DEAL.

REFERENCES

- [1] B. Ahmad, S. van der Veen, M. Fitzpatrick, and H. Guo, Residual stress evaluation in selective-laser-melting additively manufactured titanium (Ti-6Al-4V) and inconel 718 using the contour method and numerical simulation, *Addit. Manuf.* **22** (2018), 571–582.
- [2] H. Ali, H. Ghadbeigi, and K. Mumtaz, Effect of scanning strategies on residual stress and mechanical properties of Selective Laser Melted Ti6Al4V, *Mater. Sci. Eng. A* **712** (2018), 175–187.
- [3] J. B. Allen, Mesoscale modeling of metal-based selective laser melting: Evolution of the vapor capillary, *Eng. Res. Express* **3** (2021), 015026.
- [4] T. Bartel, I. Guschke, and A. Menzel, Towards the simulation of selective laser melting processes via phase transformation models, *Comput. Math. Appl.* **78** (2019), 2267–2281.
- [5] Q. Chen, X. Liang, D. Hayduke, J. Liu, L. Cheng, J. Oskin, R. Whitmore, and A. C. To, An inherent strain based multiscale modeling framework for simulating part-scale residual deformation for direct metal laser sintering, *Addit. Manuf.* **28** (2019), 406–418.
- [6] B. Coleman and W. Noll, The thermodynamics of elastic materials with heat conduction and viscosity, *Arch. Ration. Mech. Anal.* **13** (1963), 167–178.
- [7] P. Conti, F. Cianetti, and P. Pileri, Parametric finite elements model of SLM additive manufacturing process, *Procedia Struct. Integr.* **8** (2018), 410–421.
- [8] J. J. S. Dilip, S. Zhang, C. Teng, K. Zeng, C. Robinson, D. Pal, and B. Stucker, Influence of processing parameters on the evolution of melt pool, porosity, and microstructures in Ti-6Al-4V alloy parts fabricated by selective laser melting, *Prog. Addit. Manuf.* **2** (2017), 157–167.
- [9] Z. Dong, Y. Liu, W. Wen, J. Ge, and J. Liang, Effect of hatch spacing on melt pool and as-built quality during selective laser melting of stainless steel: Modeling and experimental approaches, *Dent. Mater.* **12** (2019), 50.
- [10] M. Frémond, *Materiaux a memoire de forme*, C. R. Acad. Sci. **34**(2) (1987), 239–244.
- [11] M. Galati, L. Iuliano, A. Salmi, and E. Atzeni, Modelling energy source and powder properties for the development of a thermal FE model of the EBM additive manufacturing process, *Addit. Manuf.* **14** (2017), 49–59.
- [12] R. K. Ganeriwala, M. Strantza, W. King, B. Clausen, T. Phan, L. Levine, D. Brown, and N. Hodge, Evaluation of a thermomechanical model for prediction of residual stress during laser powder bed fusion of Ti-6Al-4V, *Addit. Manuf.* **27** (2019), 489–502.
- [13] J. Goldak, A. Chakravarti, and M. Bibby, A new finite element model for welding heat sources, *Metall. Trans. B* **15** (1984), 299–305.
- [14] D. Gu, C. Ma, M. Xia, D. Dai, and Q. Shi, A multiscale understanding of the thermodynamic and kinetic mechanisms of laser additive manufacturing, *Engineering* **3** (2017), 675–684.
- [15] M. Hill and D. Nelson, The inherent strain method for residual stress determination and its application to a long welded joint, *ASME Press. Vessels Pip.*, Vol. 318, 1995, pp. 343–352.
- [16] N. Keller, *Verzugsminimierung bei selektiven Laserschmelzverfahren durch Multi-Skalen-Simulation*, Ph.D. thesis, Universität Bremen, 2017.
- [17] N. Keller and V. Ploshikhin, *New method for fast predictions of residual stresses and distortion of AM part*, Proceedings of the 25th Solid Freeform Symposium, Vol. 25, University of Texas, Austin, 2014, pp. 1229–1237.
- [18] T. A. Krol, C. Seidel, J. Schilp, M. Hofmann, W. Gan, and M. Zaeh, Verification of structural simulation results of metal-based additive manufacturing by means of neutron diffraction, *Phys. Procedia* **41** (2013), 849–857.

- [19] T. A. Krol, S. Westhäuser, M. F. Zäh, J. Schilp, and G. Groth, Development of a simulation-based process chain - strategy for different levels of detail for the preprocessing definitions, *SNE Simul. Notes Eur.* **21** (2011), 135–140.
- [20] J. Kruth, L. Froyen, J. Van Vaerenbergh, P. Mercelis, M. Rombouts, and B. Lauwers, Selective laser melting of iron-based powder, *J. Mater. Process. Technol.* **149** (2004), 616–622.
- [21] C. Li, J. Liu, X. Fang, and Y. Guo, Efficient predictive model of part distortion and residual stress in selective laser melting, *Addit. Manuf.* **17** (2017), 157–168.
- [22] X. Liang, L. Cheng, Q. Chen, Q. Yang, and A. C. To, A modified method for estimating inherent strains from detailed process simulation for fast residual distortion prediction of single-walled structures fabricated by directed energy deposition, *Addit. Manuf.* **23** (2018), 471–486.
- [23] Y. Lu, S. Wu, Y. Gan, T. Huang, C. Yang, L. Junjie, and J. Lin, Study on the microstructure, mechanical property and residual stress of SLM Inconel-718 alloy manufactured by differing island scanning strategy, *Opt. Laser Technol.* **75** (2015), 197–206.
- [24] J. G. Michopoulos, A. P. Iliopoulos, J. C. Steuben, A. J. Birnbaum, and S. G. Lambrakos, On the multiphysics modeling challenges for metal additive manufacturing processes, *Addit. Manuf.* **22** (2018), 784–799.
- [25] K. Mills, *Recommended values of thermophysical properties for selected commercial alloys*, Woodhead Publishing, Cambridge, 2002.
- [26] H. Murakawa, D. Deng, N. Ma, and J. Wang, Applications of inherent strain and interface element to simulation of welding deformation in thin plate structures, *Comput. Mater. Sci.* **51** (2012), 43–52.
- [27] F. Neugebauer, N. Keller, V. Ploshikhin, F. Feuerhahn, and H. Koehler, *Multi scale FEM simulation for distortion calculation in additive manufacturing of hardening stainless steel*, International Workshop on Thermal Forming and Welding Distortion, Vol. 54, BIAS Verlag, Bremen, Germany, 2014, pp. 1–11.
- [28] I. Noll, T. Bartel, and A. Menzel, A computational phase transformation model for selective laser melting processes, *Comput. Mech.* **66** (2020), 1321–1342.
- [29] L. Papadakis, A. Loizou, J. Risse, and J. Schrage, Numerical computation of component shape distortion manufactured by selective laser melting, *Procedia CIRP* **18** (2014), 90–95.
- [30] D. Riedlbauer, P. Steinmann, and J. Mergheim, Thermomechanical finite element simulations of selective electron beam melting process: Performance considerations, *Comput. Mech.* **54** (2014), 109–122.
- [31] M. Schänzel, A. Ilin, and V. Ploshikhin, New approach for fast numerical prediction of residual stress and distortion of AM parts from steels with phase transformations, *Math. Modell. Weld Phenomena* **12** (2019), 1–21.
- [32] M. Schänzel, D. Shakirov, A. Ilin, and V. Ploshikhin, Coupled thermo-mechanical process simulation method for selective laser melting considering phase transformation steels, *Comput. Math. Appl.* **78** (2019), 2230–2246.
- [33] C. Seidel and M. F. Zaeh, Multi-scale modelling approach for contributing to reduced distortion in parts made by laser-based powder bed fusion, *Procedia CIRP* **67** (2018), 197–202.
- [34] I. Setien, M. Chiumenti, S. Veen, M. Sebastian, F. Garcíandía, and A. Echeverría, Empirical methodology to determine inherent strains in additive manufacturing, *Comput. Math. Appl.* **78** (2019), 2282–2295.
- [35] M. Siewert, F. Neugebauer, J. Epp, and V. Ploshikhin, Validation of mechanical layer equivalent method for simulation of residual stresses in additive manufactured components, *Comput. Math. Appl.* **78** (2019), 2407–2416.
- [36] J. C. Simo and T. J. R. Hughes, *Computational inelasticity*, Interdisciplinary Applied Mathematics, Vol 7, Springer, New York, NY, 1998.
- [37] Y. Ueda, K. Fukuda, K. Nakacho, and S. Endo, A new measuring method of residual stresses with the aid of finite element method and reliability of estimated values, *Trans. JWRI* **4** (1975), 123–131.
- [38] S. Wang, M. Wei, and L. Tsay, Tensile properties of LBW welds in Ti-6Al-4V alloy at evaluated temperatures below 450°C, *Mater. Lett.* **57** (2003), 1815–1823.
- [39] A. S. Wu, D. W. Brown, M. Kumar, G. F. Gallegos, and W. E. King, An experimental investigation into additive manufacturing-induced residual stresses in 316L stainless steel, *Metall. Mater. Trans. A* **45** (2014), 6260–6270.
- [40] W. Yan, S. Lin, O. L. Kafka, Y. Lian, C. Yu, Z. Liu, J. Yan, S. Wolff, H. Wu, E. Ndip-Agbor, M. Mozaffar, K. Ehmann, J. Cao, G. J. Wagner, and W. K. Liu, Data-driven multi-scale multi-physics models to derive process-structure-property relationships for additive manufacturing, *Comput. Mech.* **61** (2018), 521–541.
- [41] M. Yuan and Y. Ueda, Prediction of residual stresses in welded T- and I-joints using inherent strains, *J. Eng. Mater. Technol.* **118** (1996), 229–234.
- [42] M. Zaeh and G. Branner, Investigations on residual stresses and deformations in selective laser melting, *Prod. Des. Eng.* **4** (2010), 35–45.
- [43] Q. Zhang, J. Xie, Z. Gao, T. London, D. Griffiths, and V. Oancea, A metallurgical phase transformation framework applied to SLM additive manufacturing processes, *Mater. Des.* **166** (2019), 107618.
- [44] Z. D. Zhang, O. Ibhádode, U. Ali, C. F. Dibia, P. Rahnama, A. Bonakdar, and E. Toyserkani, Topology optimization parallel-computing framework based on the inherent strain method for support structure design in laser powder-bed fusion additive manufacturing, *Int. J. Mech. Mater. Des.* **16** (2020), 897–923.

How to cite this article: I. Noll, T. Bartel, and A. Menzel, *On the incorporation of a micromechanical material model into the inherent strain method—Application to the modeling of selective laser melting*, *GAMM-Mitteilungen*. **44** (2021), e202100015. <https://doi.org/10.1002/gamm.202100015>